THESIS FOR THE DEGREE OF LICENTIATE OF ENGINEERING

Investigation of Process Conditions for PVDF Recovery from Spent Li-ion Batteries via Supercritical CO_2 and Co-solvent

YİĞİT AKBAŞ

Department of Chemistry and Chemical Engineering

CHALMERS UNIVERSITY OF TECHNOLOGY

Gothenburg, Sweden 2025

Investigation of Process Conditions for PVDF Recovery from Spent Li-ion Batteries via Supercritical CO_2 and Co-solvent
YİĞİT AKBAŞ

Technical report no 2025:15

Department of Chemistry and Chemical Engineering
Chalmers University of Technology
SE-412 96 Gothenburg
Sweden
Telephone + 46 (0)31-772 1000

Cover: Illustration of the supercritical CO_2 extraction process for PVDF extraction and images of the recovered PVDF.

Chalmers Digitaltryck
Gothenburg, Sweden 2025

Investigation of Process Conditions for PVDF Recovery from Spent Li-ion Batteries via Supercritical CO_2 and Co-solvent

YİĞİT AKBAŞ

Industrial Materials Recycling
Department of Chemistry and Chemical Engineering
Chalmers University of Technology

Abstract

The exponential growth in lithium-ion battery (LiB) demand for electric vehicles and portable electronics has escalated the need for efficient and sustainable recycling processes. Current industrial recycling strategies focus predominantly on the recovery of valuable transition metals such as Li, Co, Ni, and Mn, while neglecting the polymeric binder, poly(vinylidene fluoride) (PVDF), which constitutes a fraction of the electrode mass and represents a potential source of fluorine emissions when incinerated. This work investigates the separation and recovery of PVDF from the black mass of spent LiBs using supercritical carbon dioxide ($scCO_2$) with polar co-solvents such as dimethyl sulfoxide and acetone.

The study explores the effect of pressure (60 - 120 bar), temperature (30 - 90 °C), and solvent composition on PVDF solubility and extraction efficiency. The influence of process conditions identified for PVDF extraction from a complex battery waste, so-called black mass. The results demonstrated that at $X_{CO_2} \approx 0.34$ (at 80 bar, 70 °C) a balance between CO_2 density/diffusivity and co-solvent polarity yields favorable PVDF separation. Morphological analyses (SEM/EDS) reveal increased liberation of cathode active materials from graphite at lower pressures, corroborating the thermal and compositional evidence from TGA and FTIR.

The findings highlight the potential of $scCO_2$-based processes as a green and tunable alternative to conventional solvent- or heat-based PVDF removal methods. By enabling controlled binder recovery without toxic emissions, this approach supports the development of a closed-loop and fluorine-responsible recycling strategy for Li-ion batteries in line with the EU Battery Regulation 2023/1542.

Keywords: lithium-ion battery; black mass; polyvinylidene fluoride binder; recycling process; supercritical carbon dioxide extraction; thermogravimetric analysis; dimethyl sulfoxide; acetone

List of Publications and Manuscripts

This thesis is based on the following publication and manuscript:

Paper I

Y. Akbaş, M. Petranikova, B. Ebin, Co-solvent controlled PVDF extraction from spent Li-ion batteries using supercritical CO_2, Separation and Purification Technology (2025). https://doi.org/10.1016/j.seppur.2025.134056

Contribution: Main author, all experimental work and data analysis.

Paper II

Y. Akbaş, Shuichi Haraguchi, M. Petranikova, B. Ebin, Investigation of PVDF Binder Recovery from Spent Li-ion Batteries via Supercritical CO_2: Role of Pressure, Temperature and Acetone, (Will be submitted to Separation and Purification Technology)

Contribution: Main author, all experimental work and data analysis.

Abbreviations and Definitions

The following abbreviations and definitions are used throughout this thesis.

Abbreviations.	Definition
%T	Percent Transmission
°	Degree
°C	Degree Celsius
AM	Active Material
ATR	Attenuated Total Reflection
CC	Current Collector
CMC	Carboxymethyl Cellulose
CO_2	Carbon Dioxide
DEC	Diethyl Carbonate
DMAc	Dimethylacetamide
DMC	Dimethyl Carbonate
DMF	Dimethylformamide
DMI	1,3-Dimethyl-2-Imidazolidinone
DMPU	N,N′-Dimethylpropyleneurea
DSC	Differential Scanning Calorimetry
DTG	Derivative Thermogravimetry
EC	Ethylene Carbonate
EDS	Energy Dispersive X-ray Spectroscopy
EG	Ethylene Glycol
EMC	Ethyl Methyl Carbonate
EU	European Union
EV	Electric Vehicle
FTIR	Fourier-Transform Infrared Spectroscopy
GWh	Gigawatt-hours
HF	Hydrogen Fluoride
HSP	Hansen Solubility Parameter
LCO	Lithium Cobalt Oxide
Li_2O	Lithium Oxide
LiB	Lithium-Ion Battery
LiF	Lithium Fluoride
$LiPF_6$	Lithium Hexafluorophosphate
LNMO	Lithium Nickel Manganese Spinel
LMO	Lithium Manganese Oxide
LMT	Light Means of Transport
MQ	Milli-Q
N_2	Nitrogen
NaOH	Sodium Hydroxide
NCA	Lithium Nickel Cobalt Aluminum Oxide
NDIR	Non-dispersive Infrared

NiO	Nickel (II) Oxide
NMC	Lithium Nickel Manganese Cobalt Oxide
NMP	N-methyl-2-pyrrolidone
NMR	Nuclear Magnetic Resonance
P_c	Critical Pressure
PE	Polyethylene
PFAS	Per- and Polyfluoroalkyl Substances
POF_3	Phosphoryl Fluoride
PP	Polypropylene
ppb	Part Per Billion
PS	Post Separation
PTFE	Polytetrafluoroethylene
RT	Room Temperature
SBR	Styrene-butadiene Rubber
$scCO_2$	Supercritical Carbon Dioxide
SCF	Supercritical Fluid
SEM	Scanning Electron Microscope
T_c	Critical Temperature
TEP	Triethyl Phosphate
TGA	Thermogravimetric Analysis
THF	Tetrahydrofuran
UV-vis	Ultraviolet-Visible
wt.%	Weight Percentage
XRD	X-Ray Diffraction

Table of Contents

1 Introduction

Sony and Asahi Kasei introduced the first commercially available rechargeable lithium-ion battery (LiB) in 1991. Since then, LiBs have become widely adopted across numerous sectors due to their advantageous combination of high energy and power density, along with a relatively extended operational lifespan [1,2]. Owing to these features, lithium-ion batteries have played a central role in the transition to electric vehicles (EV). Today, they are widely utilized in EV, energy storage systems, and portable electronic devices such as smartphones, laptops, and tablets.

Based on the specific application requirements, LiB cells are manufactured in four main formats: cylindrical, prismatic, pouch, and coin cells. Regardless of their shape, all LiB cells are typically composed of five essential components: the cathode, separator, anode, electrolyte, and casing [3]. When the casing is removed, a layered arrangement of anode, separator, and cathode is visible, with the transparent electrolyte distributed among them. This non-aqueous electrolyte is a complex mixture that includes a conductive salt, primarily lithium hexafluorophosphate ($LiPF_6$), along with organic carbonate solvents and various additives. To ensure effective dissociation of the salt and maintain low viscosity, both polar and non-polar solvents are commonly employed [4]. The combined layered structure of the cathode, anode, and separator is referred to as the electrode stack.

In recent years, the demand for LiBs has surged, primarily due to the automotive sector's shift toward electric mobility. To meet this growing need, global battery production capacity reached 2500 gigawatt-hours (GWh) in 2023, with a 25 % increase from 2022. If all current corporate plans are executed as scheduled, worldwide manufacturing capacity is projected to surpass 9000 GWh by 2030 [5]. However, an alternative projection proposes a more moderate scenario, estimating global demand for LiB cells to reach approximately 5500 GWh by 2040 [6]. Assuming an average specific energy of 250 watt-hours per kilogram, this corresponds to an estimated total mass of 22 million metric tons of LiB cells [7].

Establishing effective recycling methods for end-of-life LiBs is essential for multiple reasons. Primarily, LiBs are considered as hazardous waste because they contain various toxic and environmentally harmful elements [8,9]. If end-of-life LiBs are left untreated, they pose a serious environmental risk through the leaching of hazardous substances into soil and groundwater. Additionally, improperly stored spent LiBs present a verified fire hazard; in the event of overheating or ignition, numerous toxic compounds are released into the air as gases

and smoke [10–12]. Beyond environmental and safety concerns, recycling plays a vital role in securing raw materials. Lithium, nickel, cobalt, manganese, copper, graphite, and phosphorus are particularly important, as they are categorized as critical raw materials due to projected demand surpassing supply in the near future [13]. The majority of these materials are extracted and refined outside of Europe, in countries such as the Democratic Republic of Congo, China, Chile, Russia, South Africa, and Australia [14]. Without a robust recycling infrastructure, the European Union's (EU's) efforts to fully electrify transportation by 2035 would remain heavily dependent on geopolitical stability [15]. Most critically, recycling and proper handling of end-of-life LiBs is a legal obligation under EU legislation established in 2006 [16]. An amendment to this directive in 2019 introduced a requirement for LiB recycling efficiency by weight to reach 70 % by 2030 [17].

After batteries reach the end of their service life, they are collected for recycling operations [18]. These processes typically involve various pre-treatment steps, which may encompass module disassembly, discharging, thermal conditioning, and mechanical methods such as shredding. Based on the recycling technique applied, these steps can be performed individually or in combination to enhance material recovery. Once shredding is complete, a separation phase is carried out to remove larger components such as casings, separators, and metal current collectors from the processed material. The residual fine-grained fraction, commonly referred to as black mass (BM), remains as the primary recyclable material [19,20].

Recovering valuable metals from black mass (BM) plays a crucial role in reducing raw material costs and promoting material circularity [21]. Although numerous studies have explored metal recovery from LiBs-BM [3,22,23], the recycling of organic components has seen limited progress due to their relatively low economic value. BM includes organic binders such as polyvinylidene fluoride (PVDF), carboxymethyl cellulose (CMC), and polytetrafluoroethylene (PTFE), which can result in hydrogen fluoride (HF) emissions and/or carbon release during high-temperature processing [24]. As mentioned before LiB demand is projected to reach 22 million tons. Given that a standard LiB cell typically contains around 3 wt.% PVDF binder [25], and 660,000 tons of PVDF from LiB waste estimated globally. Since PVDF recycling technologies are still in lab-scale, much of it ends up in low-value by-products, thereby increasing disposal costs and the risk of fluorinated compound contamination [26–28]. To establish a circular value chain, it is imperative to recycle this waste instead of relegating it to incineration or landfilling [20].

One of the major technical challenges in recycling valuable metals from spent LiBs lies in the effective separation of active materials (AM) from current collectors (CCs), typically composed of aluminum and copper, as their presence negatively affects leaching efficiency [29]. Even after successful detachment of CCs, residual PVDF adhered to AM surfaces continues to impede subsequent metal recovery processes. Various techniques have been developed for AM-CC separation, including mechanical [30–32], thermal [33–35], and chemical approaches [29,36–38]. The chemical method often employs solvents such as ionic liquids [39], molten salts [40], deep eutectic solvents [41,42] , and organic solvents [29,36–38] to facilitate binder removal and enable delamination of the AM from CCs. Among these, N-methyl-2-pyrrolidone (NMP) is a conventional choice for dissolving PVDF, though it poses ecological concerns due to its low biodegradability and environmental toxicity [38].

Overall, PVDF recovery remains a critical bottleneck in LiB recycling due to multiple factors. High-temperature treatment methods often lead to the release of hazardous substances such as hydrogen fluoride (HF) and per- and polyfluoroalkyl substances (PFAS), which pose severe risks to human health and the environment [43]. Furthermore, PVDF recycling is still underdeveloped on an industrial scale [28]; most of the binder ends up in secondary waste streams rather than being reclaimed efficiently, in the end compromising the overall recovery rate of valuable metals [27]. These limitations not only escalate the cost of battery waste management but also contribute to the environmental burden associated with fluorinated compound contamination. Hence, there is a pressing need for scalable, eco-friendly, and effective PVDF recycling strategies to advance sustainable battery recycling technologies.

Numerous laboratory-scale studies have explored organic solvent-based methods for PVDF extraction from spent LiB materials [29,37,44–46]. These solvents are either applied to intact electrodes to facilitate delamination of AM layers from CCs or to black mass (BM) for PVDF dissolution, both relying on solvent-PVDF interactions. However, the binding energy varies depending on whether the interaction occurs between AM particles or between AM and CC [47]. Among organic solvents, ethylene glycol (EG) [37], dimethylformamide (DMF), dimethylacetamide (DMAc), and dimethyl sulfoxide (DMSO) [29] have attracted attention as potential green solvents for PVDF removal at atmospheric pressure. Nonetheless, these solvents typically require elevated processing temperatures: approximately 100°C for EG, 150°C for DMF, 160°C for DMAc, and 180°C for DMSO. With EG, delamination times vary significantly with temperature, ranging from several hours at room temperature (RT) to just 6 seconds at 160 °C. Reported PVDF removal yields from BM using DMF, DMAc, and DMSO

are approximately 33, 31, and 31 wt.%, respectively, while delamination efficiencies from cathode samples are considerably higher: 93, 85, and 93 wt.%, respectively. Sarkar et al. [48] demonstrated complete separation of aluminum CC from the cathode using a tetrahydrofuran (THF):NMP (1:1 v/v) mixture at 90 ℃ within 50 minutes. Similarly, Bai et al. [36] achieved successful delamination using triethyl phosphate (TEP) at 100 ℃ for 60 minutes or 150 ℃ for 30 minutes. Using 1,3-dimethyl-2-imidazolidinone (DMI), PVDF recovery took 30 minutes for homemade cathodes but extended to 5 hours for commercial electrodes at 150 ℃ [38]. These variations emphasize that factors such as coating thickness, particle size distribution, and battery-induced impurities significantly affect processing times even under identical solvent and temperature conditions.

An emerging alternative involves supercritical fluid (SCF) technology, particularly supercritical carbon dioxide ($scCO_2$), which is favored for its low critical temperature and pressure, and its ability to dissolve polar compounds like electrolyte solvents [49,50]. However, PVDF's high molecular weight and crystallinity hinder its dissolution in pure $scCO_2$, even under extreme conditions (e.g., 300 ℃ and 2750 bar), as shown by Rindfleisch et al. [51]. Due to CO_2's low polarizability, it is ineffective in breaking down the polar interactions within PVDF at elevated temperatures [52]. Consequently, the use of co-solvents is necessary to enhance solubility.

Yim et al. [53] explored various co-solvents, DMF, NMP, DMSO, and DMAc for PVDF extraction using $scCO_2$, identifying favorable conditions with DMF as co-solvent at 80℃ and 100 bar for 20 minutes. Under these conditions, a binder removal yield of 98.8 wt.% was achieved. Though DMSO yielded slightly lower extraction rates than DMF, PVDF recovered with DMSO showed superior performance when reused in new battery cells. Fu et al. [54] also confirmed high extraction efficiency using DMSO at 70 ℃ and 80 bar in 13 minutes. Alternatively, Hayagan et al. [55] demonstrated effective delamination using a TEP:acetone (75:25 v/v) mixture at 120℃ and 100 bar for 15 minutes. These findings underline the potential of co-solvent systems in $scCO_2$ to improve both PVDF solubility and delamination efficiency.

Among tested co-solvents, DMSO emerges as a particularly promising candidate due to its polarity, miscibility with $scCO_2$ [56], and ability to retain the structural integrity of PVDF upon recycling. Its strong dipolar nature, without hydrogen bond donation, enables disruption of intermolecular forces within PVDF without degrading polymer chains [57]. Moreover, the large volume expansion (up to 200 %) of DMSO under $scCO_2$ pressure above 60 bar facilitates

PVDF precipitation after dissolution [58]. Recent studies have demonstrated that acetone whose Hansen solubility parameters (δD = 15.5, δP = 10.4, δH = 7.0 $MPa^{½}$) closely match those of PVDF, can dissolve PVDF and facilitate electrode delamination, with solubility increasing with temperature and reaching a maximum around 150 °C [59]. This establishes acetone as a volatile, relatively green solvent of particular relevance for direct PVDF recovery. Furthermore, the inclusion of a volatile co-solvent such as acetone in a mixed system is advantageous because it lowers the liquid–liquid equilibrium boundary [60–62], modifies the overall Hansen solubility parameters, and reduces system viscosity [63].

Although substantial progress has been made at the laboratory scale, supercritical CO_2 processing has not yet been applied to recover PVDF from industrial black mass, highlighting a significant gap in current research.

This study aims to bridge that gap by evaluating PVDF separation from industrial BM using $scCO_2$ in combination with DMSO/acetone as a co-solvent. The objective is to establish a single-step, low-temperature, and environmentally benign process wherein PVDF is first dissolved in the co-solvent under $scCO_2$ conditions, then successfully separated by CO_2 flushing. This approach seeks to most effective the co-solvent/BM/sc-CO_2 ratio and processing parameters to enhance recovery yield and finally contributing to the development of scalable and sustainable battery recycling technologies.

2 Background

2.1 EU directive and regulation for batteries and waste batteries

The Batteries Directive (2006/66/EC) was the first EU legislation regulating the collection, recycling, and disposal of batteries to minimize environmental impact and recover valuable materials [16]. It limited hazardous substances such as mercury, cadmium, and lead and introduced producer responsibility for end-of-life management. On 12 July 2023, Directive 2006/66/EC was repealed and replaced by Regulation (EU) 2023/1542, which governs the full life cycle of batteries within the framework of the European Green Deal and the Circular Economy Action Plan [17]. This regulation establishes strict sustainability requirements covering design, production, and waste management, aiming to enhance recycling efficiency and reduce the environmental and health impacts of battery materials.

The regulation introduces carbon-footprint declarations and minimum recycled-content targets for metals such as Co, Ni, Li, and Pb, supported by digital battery passports for traceability. It also enforces removability, durability, and due-diligence requirements for raw materials. Recycling targets are ambitious, reaching 70 % efficiency and recovery rates of 90 % Co, 50 % Li, and 90 % Ni by 2027. However, no explicit target is defined for the recovery of polymeric components such as PVDF. Article 113 prohibits energy recovery routes and prioritizes prevention, reuse, and recycling within the waste hierarchy. Moreover, Article 21 restricts the use of hazardous substances to protect human health and the environment, covering fluorinated degradation products of PVDF, including HF and PFAS, which can form during high-temperature binder removal.

2.2 Li-ion battery components and compositions

A battery pack integrated into an electrically powered vehicle comprises a predefined number of battery modules, along with various control and protection subsystems. Each battery module consists of multiple LiB cells electrically interconnected within a structural frame, which also accommodates integrated battery management electronics. LiB cells are commercially available in four shapes: cylindrical, prismatic, pouch, and coin cells, each with distinct electrochemical and mechanical characteristics suited for specific applications [64–67]. LiB cell is composed of five primary components: the cathode, anode, separator, electrolyte and a casing.

2.2.1 Cathode

The cathode comprises three key components: the current collector, the active cathode material, and a polymeric binder. The active material, typically composed of lithium metal oxides, is coated onto an aluminum foil current collector using a binder, most commonly PVDF, which ensures mechanical stability and adhesion.

Among the various cathode chemistries, six have been widely commercialized: lithium nickel manganese cobalt oxide (NMC), lithium cobalt oxide (LCO), lithium nickel cobalt aluminum oxide (NCA), lithium manganese oxide (LMO), lithium iron phosphate (LFP), and lithium nickel manganese spinel (LNMO). These materials are named according to their principal transition metal components, which influence parameters such as specific capacity, thermal stability, and cost [2,68].

2.2.2 Anode

The anode serves as the negative electrode during discharge, is typically composed of a thin copper current collector coated with an active material and bound together using polymeric binders. The most prevalent active anode material is natural or synthetic graphite due to its favorable intercalation potential, abundance, and high electrical conductivity. In certain high-rate or long-cycle applications, lithium titanium oxide ($Li_4Ti_5O_{12}$) is employed as an alternative for its enhanced structural stability and safety [2,68]. Commercial binders for the anode commonly include carboxymethyl cellulose (CMC), styrene-butadiene rubber (SBR), and, in some instances, polyvinylidene fluoride (PVDF) [69]. These binders contribute to electrode flexibility and mechanical cohesion, particularly critical in composite electrodes subjected to repeated volume changes during cycling.

2.2.3 Separator

The separator physically isolates the anode from the cathode while permitting the transport of lithium ions via the electrolyte. This dual function is essential to prevent internal short-circuiting while ensuring ionic conductivity within the cell. The LiB separator is composed of polyolefin materials such as polypropylene (PP) and polyethylene (PE), which offer chemical inertness, mechanical durability, and thermal stability up to moderate temperatures [70].

2.2.4 Electrolyte

The electrolyte in LiBs plays a critical role as the ionic conductor, enabling lithium-ion transport between the anode and cathode during charge and discharge cycles. State-of-the-art

LiB electrolytes are primarily non-aqueous liquid systems, comprising a lithium salt, most commonly lithium hexafluorophosphate ($LiPF_6$), dissolved in a mixture of organic carbonate solvents such as ethylene carbonate (EC), dimethyl carbonate (DMC), ethyl methyl carbonate (EMC), and diethyl carbonate (DEC) [71]. EC is favored for its high dielectric constant, which enhances salt dissociation and stabilizes electrode interfaces, while linear carbonates are added to reduce the viscosity and improve conductivity. $LiPF_6$ has limitations, including its thermal instability and tendency to decompose into hazardous by-products such as HF and POF_3, especially during improper recycling or high-temperature treatments [72]. Despite its shortcomings, $LiPF_6$ remains the industry standard due to its adequate electrochemical performance and compatibility with commercial battery components [73].

2.2.5 Binders

In LiBs, binders are essential components of both electrodes, ensuring mechanical cohesion and adhesion of the active materials to the current collectors. The binder forms a matrix that stabilizes the electrode structure and maintains integrity during repeated charging and discharging cycles. Commonly used binders include polyvinylidene fluoride (PVDF), carboxymethyl cellulose (CMC), and styrene-butadiene rubber (SBR) [74]. Among these, PVDF stands out as the predominant binder material, particularly in commercialized cathodes and some anodes, due to its strong chemical stability, electrochemical inertness, and compatibility with N-methyl-2-pyrrolidone (NMP) solvent-based electrode processing [75].

PVDF, a semi-crystalline fluoropolymer, offers superior thermal and oxidative stability, which is vital for high-performance battery operation and safety [76]. PVDF exhibits several crystalline phases, including α, β, and γ, which differ in chain conformation and dipole alignment. Among these, the β-phase is particularly desirable for battery applications because of its strong piezoelectric and ferroelectric properties, providing excellent adhesion, mechanical stability, and chemical resistance in the electrode composite. The high dielectric constant and electrochemical stability against organic electrolytes make it a preferred binder material in lithium-ion batteries, ensuring efficient ion transport and good electrode integrity during cycling. However, its high decomposition temperature and fluorine content pose significant challenges during recycling. Upon thermal treatment, PVDF decomposes to release hazardous compounds such as hydrogen fluoride (HF) and various organofluorides, which are toxic and corrosive [77]. As observed in studies involving pyrolysis and incineration, the decomposition of PVDF facilitates the separation of electrode active materials from metal foils,

aiding in mechanical delamination processes [28,78]. Nonetheless, this also leads to the formation of fluorine containing by-products, raising environmental and occupational safety concerns. Therefore, while PVDF contributes to the performance of long-lasting LiBs, its removal and decomposition require careful handling in end-of-life battery processing, prompting a push for alternative binder systems that balance functionality and sustainability.

It is also worth mentioning the binder additives to enhance mechanical stability, electronic conductivity, and electrode durability. SBR is widely used in anodes due to its excellent elasticity, which accommodates the volume changes of graphite during cycling, reducing the risk of cracking and delamination [79]. CMC acts as both an anode binder and dispersant, providing hydrophilicity and strong adhesion to graphite particles while enabling the use of water-based slurries, thus offering an environmentally friendly alternative to PVDF-based systems [80]. Super P, a conductive carbon black additive, improves the electronic conductivity of the electrode by forming conductive pathways between active material particles and PVDF chains, essential in both anodes and cathodes [81]. Polytetrafluoroethylene (PTFE) is used in some specialty systems as a chemically inert binder that provides high thermal stability and structural integrity, especially under harsh cycling conditions [82]. Lithium polyacrylate serves as a multifunctional additive and binder, particularly in silicon-based anodes, where it provides strong adhesion, pH buffering, and enhanced cycling performance due to its ability to maintain structural cohesion during large volume changes [83].

2.3 Recycling of Li-ion batteries

State-of-the-art LiB recycling technologies are based on two main approaches: pyrometallurgy and hydrometallurgy [84–86]. In pyrometallurgical processes, LiB discharges, then entire cells or modules are subjected to high-temperature treatment, resulting in the formation of a metallic alloy composed primarily of Co, Cu, Fe, and Ni. This alloy is subsequently processed to recover the individual metals. During the treatment, toxic and environmentally hazardous gaseous emissions such as HF are released, while components including the separator, binder, electrolyte, and graphite undergo evaporation, decomposition, or combustion [87]. The residual slag is enriched in Al, Mn, and Li, elements that are difficult to separate individually through hydrometallurgical means and therefore are generally diverted to other industrial applications.

Hydrometallurgy is initiating with a pre-treatment stage in which LiBs are discharged, dismantled, sorted, crushed, shredded, and thermally processed into a BM containing both cathode and anode materials. This BM is then subjected to leaching, solvent extraction, ion

exchange, and related processes to recover valuable metals such as Li, Mn, Ni, Al, and Co. In certain cases, a thermal pre-treatment is employed to remove the electrolyte and/or binder, thereby improving the hydrometallurgical recovery [84,88]. Such pre-treatments are often performed under inert atmospheres (e.g., N_2) to stabilize volatile electrolyte components and prevent uncontrolled reactions with oxygen and moisture.

Each method exhibits distinct advantages and limitations. Pyrometallurgy is comparatively straightforward but non-selective, requires substantial energy input, and necessitates additional treatment of hazardous off-gases. Hydrometallurgy, by contrast, enables higher recovery efficiencies for specific metals but relies on complex pre-treatment operations to achieve favorable yields. Consequently, many contemporary recycling strategies favor hydrometallurgy, aiming to maximize material recovery while simultaneously mitigating environmental impact.

2.4 Recovery approaches for PVDF binder

Thermal methods such as pyrolysis/incineration are widely applied as pre-treatment routes for PVDF removal in spent LiBs. During pyrolysis under inert gas, PVDF binder and other organics decompose between around 200 - 700 °C, leading to detachment of the active mass from current collectors and partial reduction of transition-metal oxides by carbonaceous species [89]. This improves subsequent leaching yields in hydrometallurgical steps by increasing solubility of reduced phases (e.g., Li_2O, Co, NiO) [29,90]. Incineration in air is more efficient in removing organics, but at high temperature it may also oxidize current collectors and promote formation of more oxidized phases, sometimes limiting lithium extraction efficiency. As mentioned before, both approaches generate gaseous by-products, including HF from PVDF decomposition. Overall, thermal treatment is effective for liberating black mass but is energy-intensive and environmentally sensitive due to fluoride emissions. In addition, recovery cannot be made through energy conversation anymore according to the EU battery recycling regulation [17].

An alternative route is the direct dissolution of PVDF binder using organic solvents [29,37,44–46]. Conventional choices include polar aprotic solvents such as NMP, DMF, or DMAc, which dissolve PVDF effectively, but greener alternatives such as DMSO, ionic liquids, or deep eutectic solvents are increasingly investigated. These processes can achieve high binder removal (> 85 - 90 wt.%), thereby cleanly separating active material from foils without damaging crystal structures. Solvent-based processes are particularly attractive for direct

recycling strategies, where the preserved cathode powders may be directly re-lithiated and reused. However, challenges remain in solvent cost, toxicity, recyclability, and in the purity control of re-precipitated PVDF. Scaling solvent recovery and minimizing environmental burden are therefore critical to industrial deployment.

Chemical approaches use alkaline solutions or strong nucleophiles to induce dehydrofluorination of PVDF, weakening adhesion and facilitating liberation of the active material [91]. Laboratory studies demonstrate that bases such as NaOH or alkoxides can efficiently debond electrode coatings and even recover fluoride species as stable inorganic salts. Alkaline treatment also improves hydrometallurgical leaching efficiency by eliminating fluorinated organics that otherwise interfere with downstream processes. This route is relatively low-cost and operates at moderate temperatures, but it requires careful process control to prevent excessive attack on valuable active materials and to ensure environmentally safe management of fluorine-containing effluents.

$scCO_2$, often modified with small volumes of polar co-solvents such as DMSO, has recently emerged as a promising binder-removal technology [54,92,93]. Under relatively mild conditions (~70 °C, 70 - 90 bar), $scCO_2$ penetrates electrode structures and assists in solubilizing or plasticizing PVDF, leading to rapid delamination. Compared to conventional solvents, this method minimizes liquid waste since CO_2 is easily depressurized and recycled. Studies show efficient binder removal and potential recovery of PVDF in re-usable form, though extraction performance is highly dependent on co-solvent type and dosage. Equipment requirements (high-pressure reactors) and limited large-scale demonstrations remain current barriers, but the process aligns well with green chemistry principles.

Each PVDF recycling method offers unique advantages and drawbacks. Thermal treatment is technically robust and compatible with mixed chemistries but energy-intensive and prone to HF emissions. Solvent dissolution preserves active materials and enables high-purity separation but raises sustainability concerns due to solvent recovery and toxicity. Alkaline debonding is inexpensive and effective at moderate conditions, yet managing fluorinated effluents remains critical. $scCO_2$ extraction is environmentally attractive with low solvent residues and fast kinetics, but needs for process optimization. In practice, thermal pre-treatment is currently most industrially established, while solvent- and $scCO_2$-based processes are promising for direct recycling and circular recovery of PVDF. Future advances will likely

combine these methods, balancing efficiency, environmental safety, and economic viability in integrated LiB recycling flowsheets.

3 Theory

3.1 Supercritical carbon dioxide process

$scCO_2$ is considered non-toxic, making it a potential candidate for use in the production of consumable items such as pharmaceuticals and food products [94]. Additionally, it is already employed in a range of established processes [95], including extraction procedures [96], nanoparticle synthesis and surface modification [97–100], and polymer processing applications [101–104]. One of the appealing features of supercritical fluids is their adjustable solvent characteristics, which can be modulated through changes in temperature and pressure. In the case of CO_2, reaching supercritical conditions is relatively straightforward, with a critical temperature (T_c) of 31.1 °C and a critical pressure (P_c) of 73.8 bar [105]. Despite these advantages, $scCO_2$ possesses several physicochemical limitations as a solvent. Specifically, it exhibits low viscosity, a low dielectric constant [106] and low surface tension relative to commonly used solvents. Furthermore, due to the linear structure and lack of a permanent dipole moment in CO_2 molecules, it faces significant challenges in solubilizing polar and ionic compounds [107]. In general, supercritical fluids (SCFs) exhibit unique properties compared to conventional solvents, combining the solvation capabilities of liquids with the high diffusivity and low viscosity typical of gases. Close to the critical point, even minor adjustments in temperature or pressure can cause substantial variations in properties such as solubility, partition coefficients, dipole moments, and dielectric constants. These characteristics can be readily tuned, as slight changes in temperature or pressure near the critical point allow for precise modulation of solvent strength and reactivity in material processing applications [105].

3.2 Co-solvent selection

3.2.1 Hansen solubility parameter

The Hansen Solubility Parameter (HSP) is a scientific three-dimensional numerical model used to predict the solubility behavior of materials particularly polymers, solvents, and nanoparticles by understanding how molecular interactions influence mixing or dissolution. The total cohesive energy density is divided into three intermolecular interaction components: dispersion forces (δD), polar interactions (δP), and hydrogen bonding (δH), and each expressed in units of $MPa^{1/2}$. These parameters represent the contributions of London dispersion forces, dipole–dipole interactions, and hydrogen bonding capability, respectively. Every material can be described by a unique (δD, δP, δH) triplet, and the solubility or miscibility between two

substances is evaluated by calculating the HSP distance (R_a), (Eq. 1), which is the Euclidean distance between their parameter sets in three-dimensional space. A smaller Ra indicates a higher likelihood of solubility or compatibility. The HSP model is widely applied in the formulation of polymers, coatings, solvents, and battery materials to guide molecular design and optimize performance without relying solely on experimental screening [108].

$$R_a^2 = 4\,(\delta_{D2} - \delta_{D1})^2 + (\delta_{P2} - \delta_{P1})^2 + (\delta_{H2} - \delta_{H1})^2 \quad \text{(Eq. 1)}$$

An optimal solvent should efficiently dissolve the PVDF binder while simultaneously enabling straightforward separation of the dissolved PVDF from the solvent. The Hansen solubility parameters of PVDF, as measured by Bottino et al. [61], are reported to be $\delta D = 17.2\ MPa^{1/2}$, $\delta P = 12.5\ MPa^{1/2}$, and $\delta H = 9.2\ MPa^{1/2}$, respectively.

A variety of candidate solvents have been identified for the dissolution or swelling of PVDF. These solvents can be classified based on environmental impact rankings, swelling efficacy, and their classification as dipolar aprotic solvents (characterized by high dipole moments and an inability to donate hydrogen bonds).

Bottino et al. [61] listed acetaldehyde, acetic acid, acetonitrile, acetophenone, acetyl chloride, aniline, benzyl alcohol, n-butyl acetate, γ-butyrolactone, cyclohexanol, cyclohexanone, 1,2-dibromoethane, di-n-butyl phthalate, diethyl ketone, diethyl phthalate, ethylene glycol, ethyl formate, ethyl lactate, formamide, formic acid, glycerol, mesityl oxide, methanol, methyl acetate, methyl ethyl ketone, methyl isobutyl ketone, nitromethane, 2-nitropropane, 1-propanol as good swelling agent (GSA). Common solvents used for separation processes such as water, 1-propanol, ethanol, 1-butanol, acetone, ethyl acetate, dodecane, methanol, 2-propanol, decane, ethyl lactate, 1-octanol are listed as having low risk to environment [109,110]. On the other hand, DMSO, sulfolane, acetonitrile, DMF, DMAc, NMP, N,N′-Dimethylpropyleneurea (DMPU), DMC, EC, PC, dihydrolevoglucosenone (Cyrene) are dipolar aprotic solvents which can dissolve polar and non-polar molecules. NMP, acetone, DMSO, DMF, ethylene glycol, DMAc, THF, TEP, are commonly investigated for PVDF dissolution.

3.3 Mole fraction of carbon dioxide

Changing co-solvent, co-solvent volume, pressure and temperature change the mole fraction of the experimental setup. It is a key parameter because it controls the solvent density/polarity and phase behavior, and therefore, the solvation power, selectivity and extraction kinetics [111]. Higher CO_2 mole fraction usually gives more "CO_2-like" (nonpolar, low-dielectric) solvent properties and favors extraction of nonpolar, low-molecular weight species; lower CO_2 mole

fraction increases polarity due to polar co-solvent and can enable dissolution of more polar or ionic species. To determine the CO_2 mole fraction, the densities of CO_2 at specific pressure and temperature conditions, the solvent, and BM were employed. Subsequently, the moles of CO_2 and solvent were computed using (Eq. 2), where n represents the number of moles, V the volume, ρ the density of CO_2 or the solvent and MW the molecular weight.

$$n = \frac{V \cdot \rho}{MW} \quad \text{(Eq. 2)}$$

For co-solvent/CO_2 mixtures, the mole fractions were determined using the (Eq. 3), where n represents the number of moles of each component, and the sum of the solvent and CO_2 mole fractions ($X_{co\text{-}solvent} + X_{CO_2}$) equals 1.

$$X_{CO_2} = \frac{n_{CO_2}}{n_{co\text{-}solvent} + n_{CO_2}} \quad \text{(Eq. 3)}$$

4 Experimental

4.1 Black mass preparation

In this study, black mass (BM) was employed as the primary material, sourced via mechanical treatment of EV LiBs by TES SBS France (SK TES group). The acquired BM was first manually sieved using a 500 µm mesh to remove larger fragments, such as separator and residual plastic components originating from the battery casing. Subsequent to sieving, the BM was washed with milli-Q (MQ) water (7 ppb, 18.2 MΩ·cm at 25 ℃). For this process, 100 g of BM was stirred with 5 liters of deionized water using a magnetic stirrer operating at 750 rpm under ambient temperature conditions for a duration of 14 days (Paper-I). Following the washing procedure, the suspension was filtered using a paper filter (Whatman, 1001-125) positioned within a suction filtration setup comprising a Büchner funnel and an Erlenmeyer flask. The washed BM was then dried in an oven at 60 ℃ overnight. To ensure representativeness for subsequent analysis, four sub-samples were obtained from the dried BM employing the quartering method. These sub-samples were subjected to thermogravimetric analysis (TGA) to identify the components in BM. For the second batch (Paper-II), the same manual sieving procedure was applied. A total of 127 g of BM was washed using 6.7 liters of deionized water. The washing was conducted stepwise by replacing 700 - 800 ml of water each day. The suspension was stirred at 500 rpm in a 1-liter glass bottle overnight and allowed to settle for two hours on the following day. The supernatant was then decanted, and fresh deionized water was added. This procedure was repeated for ten consecutive days. Then the same drying procedure was applied. A schematic representation of the experimental workflow is provided in Figure 1.

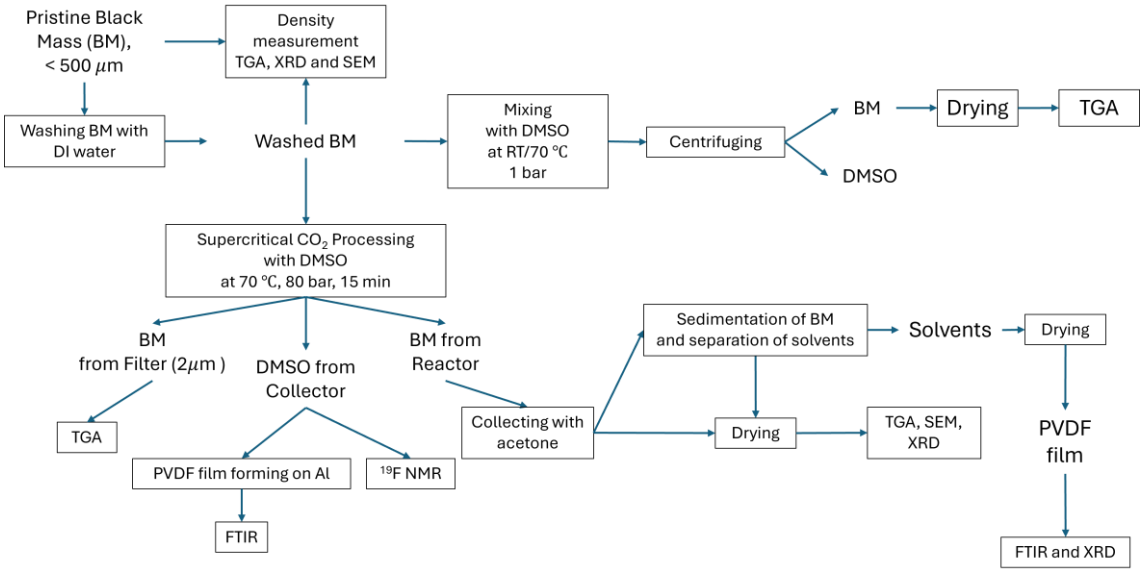

Figure 1. Flow chart of the experimental procedure.

4.2 PVDF removal at atmospheric and high pressure

The removal of PVDF from BM under atmospheric conditions was investigated at RT and at 70 °C to evaluate and compare the results with $scCO_2$ treatment. For the experiments conducted at atmospheric pressure, 1 g of pre-washed BM was placed in a beaker and mixed with 4 ml of DMSO for 18 days at RT. This procedure was performed in triplicate. Following the extraction, the samples were centrifuged at 6000 rpm for 20 minutes to facilitate the separation of the majority of DMSO from the BM. The remaining residues were subsequently dried in an oven at 60 °C overnight to ensure complete removal of DMSO. A parallel procedure was conducted at 70 °C for a duration of 24 hours.

For the $scCO_2$ treatment, a custom-built setup was employed, comprising a syringe pump (ISCO 260D, Teledyne ISCO) for the delivery of pressurized CO_2 (Air Liquide, 99.9 %, ≤ 5 ppm w/w H_2O), a thermostat (Model F10 & CM, Julabo), a stainless steel reactor (11.5 ml, equipped with a 2 µm inlet filter), Swagelok filters (2 µm and 0.5 µm) post-reactor, and a sample collection vial at the gas outlet. CO_2 was transferred through SS-316 stainless steel pipelines to the reactor, which was also fabricated from SS-316 and heated to the desired temperature via a thermostat (Model F12 & ED, Julabo). Temperature was monitored using a thermocouple attached to the top of the reactor and connected to a data logger (TC-08, Pico Technology). Pressure was monitored by a manometer positioned after the filtration system. To prevent freezing at the outlet, the exhaust metering valve was thermostatically maintained at 45 ± 5 °C.

In each experiment (Paper-I), 1 g of washed BM was introduced into the reactor together with 3 - 7 ml of DMSO (Sigma-Aldrich, ≥99.9 % purity) as co-solvent. After sealing and assembling the system, the reactor was heated to 70 °C and pressurized CO_2 was introduced until the desired conditions were achieved. The system was maintained for 15 minutes, after which the exhaust valve was opened, and 115 ± 3 ml of CO_2 at 70 °C and 80 bar was flushed through the system to transfer the DMSO with dissolved PVDF into the collector vial. Samples were then recovered from the reactor, filter (2 µm), and collector. To recover material from the reactor, acetone (EMSURE®, Merck) was used as a rinse solvent. All experiments were conducted in triplicate.

Collected samples contained processed BM along with DMSO and acetone residues. These solvents were separated (post-separation, PS) then subsequently evaporated in an oven at 60 °C for overnight. The dried BM was then subjected to thermogravimetric analysis (TGA) to quantify the extent of PVDF removal.

The same experimental methodology was also employed (Paper-II) using a co-solvent mixture of DMSO and acetone (50:50 v/v) under scCO_2 conditions at 70 °C and 120 bar for 15 min with PS. However, this setup includes only one Swagelok filter (2 µm) before the pressure meter. Temperature parameter was also investigated by using DMSO/acetone mixture at 120 bar for 15 mins. Additionally, to investigate the effect of pressure on the process, a pressure scan was performed using 4 ml of DMSO at a constant temperature of 70 °C for 15 minutes, with pressures varied across 60, 80, 120, and 140 bar.

4.3 Measurements and characterization

Thermogravimetric (TG) analysis was conducted to assess the extent of PVDF removal from various BM samples, including pristine BM, washed BM, BM collected from filter-2, and dried recovered BM from the reactor. TG measurements were performed using a TA Instruments Q500 system under a nitrogen (N_2) flow rate of 100 ml/min. The samples were heated to 700°C at a rate of 5 °C/min in high-resolution mode (resolution: 4 and sensitivity: 4), which adjusts the heating rate in response to the weight loss rate to ensure accurate correlation between mass loss and temperature. Following the heating phase, an isothermal stage of 30 min was applied at the target temperature, and the samples were subsequently cooled to RT.

The PVDF removal efficiency was determined using (Eq. 4), where R represents the recovery efficiency (wt.%) of PVDF extracted from BM, and m_0 and m_1 denote the initial and remaining

PVDF content in the BM, respectively. Standard deviation values from individual replicates were used to generate error bars.

$$R = \frac{(m_0 - m_1)}{m_0} \cdot 100 \qquad \text{(Eq. 4)}$$

A mass balance analysis was conducted to determine the distribution of DMSO and BM across different sections of the experimental apparatus. For this purpose, the reactor, filters, and collection vessels were weighed before and after each experiment using a VWR analytical balance (SM2285Di, d = 0.01 mg). TG analysis was also performed on BM collected at filter-1 to quantify the remaining DMSO content. The total weight change in the filter was used to infer the amount of BM trapped, under the assumption that the BM passage through the 0.5-micron filter was negligible. Consequently, any residual mass within the reactor was attributed exclusively to DMSO.

PVDF content in BM was quantitatively determined by measuring the total carbon content using a LECO CS744 carbon/sulfur analyzer. The BM were dried at 200°C for 3 hours under nitrogen atmosphere. In this method, BM was combusted in a high-temperature furnace under a pure oxygen atmosphere to ensure complete oxidation of carbon-containing compounds. The resulting CO and CO_2 gases were detected by a non-dispersive infrared (NDIR) detector, and the total carbon content was quantified. Assuming PVDF, carbon black and graphite as the primary carbon source, its content was tested to be calculated based on the known carbon fraction in the PVDF structure. Measurements were performed in triplicate to ensure accuracy and reproducibility.

To determine the presence of PVDF in DMSO recovered from the $scCO_2$ process, ^{19}F nuclear magnetic resonance (NMR) spectroscopy was employed using a 600 MHz Oxford magnet equipped with a Bruker NEO console and 5 mm QCIP probe. The measurements were performed with a transmitter frequency offset of -100 and 128 scans.

Fourier-transform infrared spectroscopy (FTIR) with attenuated total reflection (ATR) attachment (PerkinElmer Spectrum Two) was used to evaluate phase changes. A commercial PVDF reference sample was used for comparison. FTIR samples were prepared by depositing 50 µL of the recovered DMSO onto aluminum foil, followed by drying at 60 °C overnight to allow DMSO evaporation and PVDF film formation.

BM density was measured using a Micromeritics AccuPyc II 1340 gas pycnometer to calculate the mole fraction of CO_2 during the $scCO_2$ process. Triplicate measurements, each consisting

of 10 sub-measurements, were carried out on both pristine and washed BM samples. The resulting standard deviation was less than 0.011 g/cm³.

X-ray diffraction (XRD) analysis was conducted using a Bruker D8 Discover diffractometer with Cu-Kα radiation (λ = 1.5406 Å). The instrument operated at 40 mA and 40 kV, scanning over a 2θ range of 10° to 80°, with a scanning rate of 2°/min and a step size of 0.02°.

Morphological and structural characterizations were performed using scanning electron microscopy (SEM, FEI Quanta 200 ESEM FEG), coupled with energy-dispersive X-ray spectroscopy (EDS, Oxford Instruments X-max 80). Imaging was performed under a high vacuum with a secondary electron detector at 15 kV. Elemental mapping, when applicable, was used to analyze fluorine (F) distribution.

Differential scanning calorimetry (DSC) analysis was conducted using a Mettler Toledo DSC 5+ instrument to characterize the melting behavior of pristine PVDF powder and PVDF in its solvent-containing state (1 wt.% PVDF dissolved in 4 ml DMSO). A 2.23 mg portion of PVDF powder was placed in a closed aluminum pan equipped with a small pinhole, whereas 40.10 mg of the PVDF - DMSO mixture was sealed within a medium-pressure stainless-steel crucible (rated up to 2 MPa) to prevent solvent evaporation. The samples were subjected to a heating cycle from RT to 200 °C at a rate of 2 °C/min under a constant nitrogen flow of 50 ml/min, followed by controlled cooling to -80 °C at the same rate. Each measurement was carried out over two heating - cooling cycles, and empty crucibles were used as reference samples accordingly.

5 Results and Discussion

5.1 Characterization of the reference PVDF

Reference PVDF powder was investigated by TGA and plotted in Figure 2. Under different atmospheres reveals distinct decomposition behaviors depending on the presence of oxygen. Under a nitrogen atmosphere, PVDF exhibits a single major decomposition event, with the maximum degradation rate occurring around 385 °C, indicating a one-step thermal decomposition process typical for inert conditions. The total mass loss under nitrogen reaches 70.76 wt.% up to 700 °C, suggesting partial degradation with the formation of stable carbonaceous residues. Conversely, in a synthetic air environment, the thermal stability of PVDF increases, with the main decomposition peak shifting to approximately 412 °C, accompanied by additional oxidation peaks at around 430 °C and 441 °C. These secondary peaks indicate multi-step oxidative degradation involving further breakdown of intermediate carbon–fluorine fragments. The overall mass loss under air rises substantially to 98.81 wt.%, signifying almost complete oxidation of the polymer backbone. This comparison highlights that oxidative conditions promote both higher decomposition temperatures and more complete volatilization of PVDF residues compared to inert atmospheres.

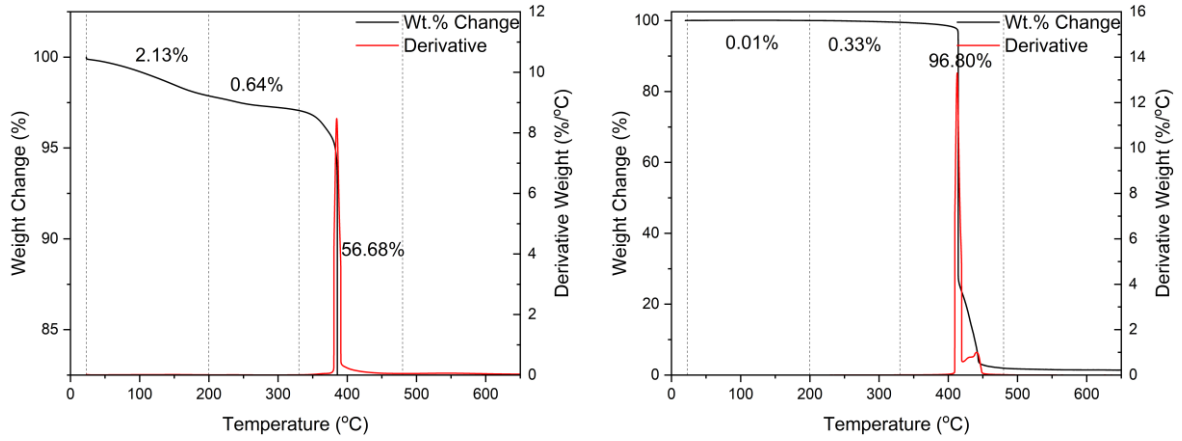

Figure 2. TGA curve of reference PVDF under **a)** nitrogen and **b)** synthetic air atmosphere.

5.2 Characterization of black mass

Total carbon analysis was employed to quantify the PVDF content in the BM by determining the weight percentages of carbon (C) and sulfur (S). Results were tabulated on Table 1. Prior to analysis, the BM was subjected to drying at 200 °C for 3 hours to eliminate electrolyte salts and residual solvents, thereby ensuring that only CMC, PVDF and graphite remained as the primary carbon sources. The aim of the measurement was enabling a more accurate estimation

of the PVDF content before and after the $scCO_2$ treatment. Initial measurements revealed that the industrial BM contained 39.07 wt.% (± 1.22) carbon, with sulfur levels being negligible. However, the relatively high standard deviation of the carbon content complicates the accurate quantification of PVDF, particularly since its content is approximately 3 wt.% and carbon constitutes about 37.5 wt.% of the PVDF molecular structure. Consequently, the carbon contribution from PVDF accounts for roughly 1.125 wt.% of the total mass, therefore, this method was not suitable to characterize PVDF quantitatively since standard deviation was 1.22.

Table 1. Carbon and sulfur weight percentage of BM.

Dried BM	Measurement-1	Measurement-2	Measurement-3	Average	Standard Deviation
Sample Mass (g)	0.0285	0.0285	0.0251	0.0274	0.0020
C wt.%	40.4	38.8	38	39.07	1.22
S wt.%	0.095	0.0783	0.0876	0.09	0.01

The sample preparation for $scCO_2$ process initiated with sieving of the industrial black mass (BM) to remove oversized residues from shredding, primarily consisting of plastic casing and separator fragments. This step was followed by a washing procedure aimed at removing residual electrolytes and the anode binder. These pre-treatment steps were essential for accurately assessing PVDF binder recovery; otherwise, the inherent heterogeneity of industrial waste complicates the quantification of PVDF extraction. Additionally, the bulk density of BM was measured to calculate the molar fraction of CO_2 in the $scCO_2$/DMSO/BM ternary system. The density of BM following sieving was determined as 3.12 g/cm^3 (after drying at 130℃ for 3 h), increasing to 3.32 g/cm^3 post-washing.

TGA was conducted in triplicate on both pristine and washed BM samples to evaluate their compositional changes with temperature. The TG curves for pristine and washed BM under a nitrogen (N_2) atmosphere are presented in Figure 3a and Figure 3b, respectively. Characteristic thermal events were identified: electrolyte-related mass loss at ~100 ℃ [112], ethylene carbonate/electrolyte residues at ~228 ℃ [113], decomposition of carboxymethyl cellulose (CMC) near 285 ℃ [114–116], and PVDF degradation around 460 ℃ [117]. Based on these, three thermal regions were defined: RT - 200 ℃ (Region-1), 200–375℃ (Region-2), and 375 - 510 ℃ (Region-3), demarcated with dashed lines in Figure 3. a and Figure 3. b.

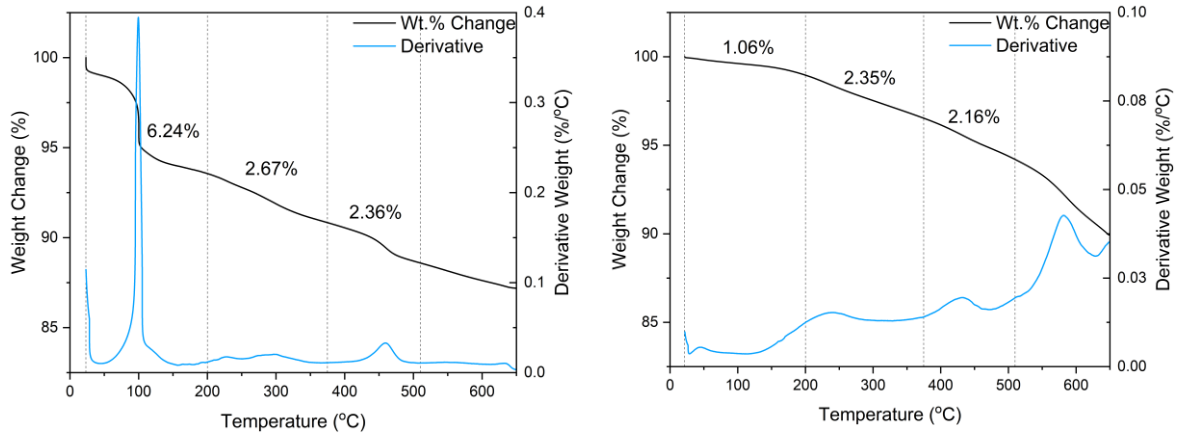

Figure 3. TG analysis of BM (in N_2 atmosphere) **a)** before and **b)** after washing with DI water (Paper-I).

For pristine BM, the average mass losses in regions-1, 2, and 3 were 6.24 % (± 0.53), 2.67 wt.% (± 0.13), and 2.36 wt.% (± 0.11), respectively (Paper-I). Under inert N_2 atmosphere, reference PVDF shows 70 wt.% mass loss by 700 °C [118]. Based on this, the recalculated PVDF content in pristine BM was found to be 3.37 wt.% (33.71 mg per g of BM). Likewise, washed BM was analyzed in triplicate (see Figure 3b), yielding mass losses of 1.06 wt.% (± 0.12), 2.35 wt.% (± 0.05), and 2.16 wt.% (± 0.15) across the same regions. The disappearance of DTG peaks near 100 °C and 285 °C (Figure 3b) signifies effective removal of electrolyte and water-soluble CMC binder via washing. Post-washing, PVDF constituted 2.16 wt.% of the BM, equating to a normalized value of 30.8 mg/g. Notably, a new thermal event emerged at around 585 °C after washing, potentially attributed to carbon black (CB) [51]. This shift to lower temperature is likely due to the increased surface area of CB following CMC elimination.

Another batch of BM (Paper-II) was also characterized in the same manner as mentioned above and plotted in Figure 4a and Figure 4b for washed BM. Temperature intervals of the regions were slightly different with the new batch and washed BM from this new batch. Region-1 (RT - 200 °C) falls in the same interval. Meanwhile region-2 falls between 200 - 330 °C and 200 - 300 °C for BM and washed BM, respectively. Region-3 falls between 330 - 480 °C and 300 - 450 °C for BM and washed BM, respectively.

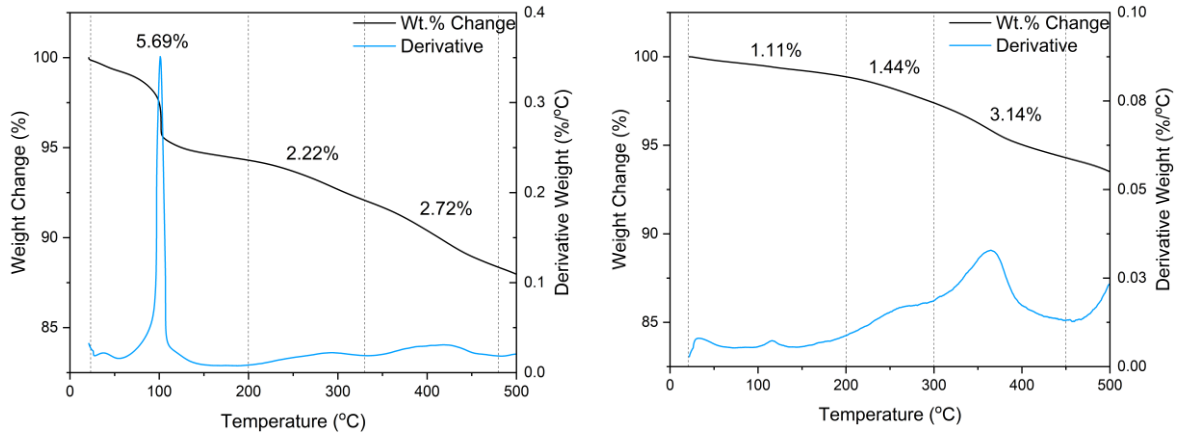

Figure 4. TG analysis of BM (in N_2 atmosphere) **a)** before and **b)** after washing with DI water (Paper-II).

For pristine BM, the average mass losses in regions-1, 2, and 3 were 5.889 wt.% (± 0.14), 2.206 wt.% (± 0.02), and 3.707 wt.% (± 0.03), respectively. Likewise, washed BM was analyzed in triplicate (see Figure 4b), yielding mass losses of 1.109 wt.% (± 0.05), 1.438 wt.% (± 0.05), and 3.141 wt.% (± 0.04) across the regions.

5.3 PVDF removal at atmospheric pressure

Control experiments were conducted under atmospheric pressure to evaluate PVDF removal from BM at RT and 70 °C. In these experiments, washed BM was mixed with DMSO for 18 days at RT in triplicate. Following this, the mixtures were centrifuged to facilitate phase separation and subsequently dried to remove residual DMSO. A similar protocol was employed at 70 °C with a contact time of 24 h (single experiment). The initial PVDF amount was 33.71 mg per gram of BM. The extent of residual PVDF in treated BMs was quantified via TGA, and results are presented in Figure 5. The analysis indicated that 29.99 mg (± 1.04) and 21.31 mg of PVDF remained after treatment at RT and 70 °C, respectively. These findings suggested negligible amount of PVDF removed at RT (after 18 days) and 30.8 wt.% of PVDF at 70 °C (after 24 h).

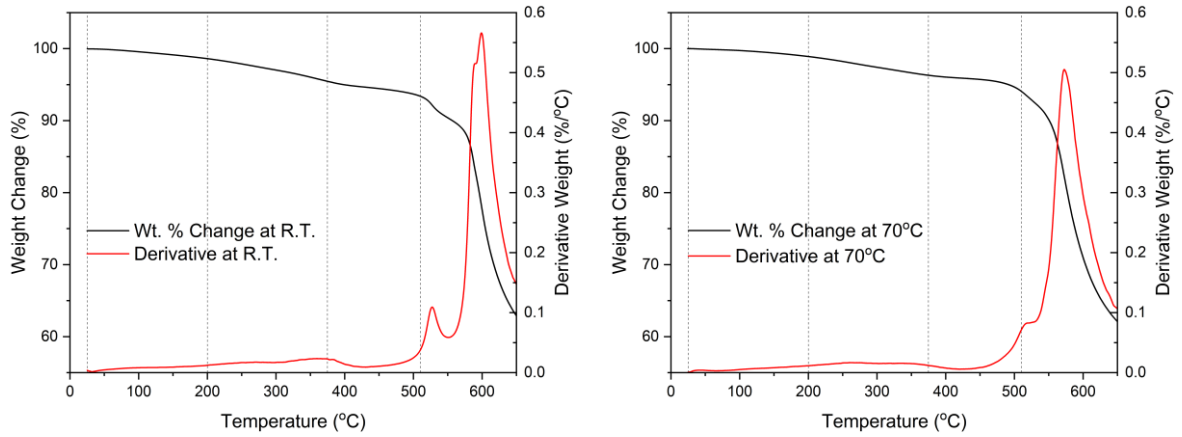

a) **b)**

Figure 5. TGA of BM processed under atmospheric conditions **a)** RT and **b)** 70 ℃.

5.4 PVDF removal at high pressure

The washed BM was subjected to $scCO_2$ extraction as outlined in the experimental section. Mass distribution assessments were carried out across various system components, namely the reactor, filter-1, filter-2, and collector, for BM, co-solvent, and PVDF. The quantity of recovered DMSO was determined through a combination of TGA and gravimetric balance. BM particles occasionally detected in the collector DMSO were excluded from calculations. DMSO and BM mass distributions are plotted in Figure 6a and Figure 6b, respectively. Increasing the co-solvent volume from 4 to 7 ml resulted in enhanced DMSO recovery efficiency, rising from 50.6 to 76.4 wt.%. The residual DMSO within the reactor were recorded as 12.3, 26.3, 28.9, 32.7, and 24.3 wt.% for respective initial volumes of 3, 4, 5, 6, and 7 ml.

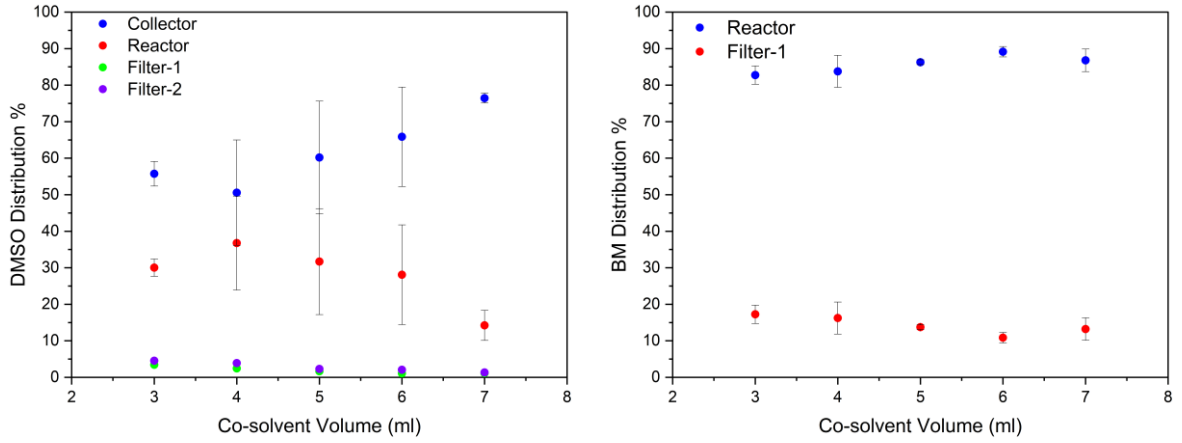

a) **b)**

Figure 6. Mass distribution of **a)** DMSO and **b)** BM after the process.

Furthermore, more than 80 wt.% of the washed BM was retained in the reactor, while the remainder accumulated in filter-1. Filter-2 contained only DMSO residue (0.1 - 0.17 g). TGA

of collected BM from filter-1 revealed the presence of 37.51 wt.% (± 0.68) DMSO and 1.05 wt.% (± 0.12) PVDF. However, due to limitations in TGA resolution, PVDF estimations in DMSO and filter-1 samples are considered to have high uncertainty. Therefore, only the reactor-remained BM was used in PVDF recovery yield calculations.

The recovery of PVDF was quantitatively evaluated by determining the residual PVDF content in the processed BM which remained within the reactor. The experiments were conducted in triplicate, and each sample was analyzed using TGA, with the results presented in Figure 7a. The derivative thermogravimetric curves (weight change rate, wt.%/°C) for samples treated with varying volumes of co-solvent was plotted in Figure 7b. Analytical comparison was focused on the region corresponding to the thermal decomposition of PVDF (Region-3), as this range distinctly represent the PVDF degradation behavior. The data clearly indicated that treatment with 4 ml of co-solvent resulted in the lowest residual PVDF content in the reactor (21.79 mg, ± 0.38), corresponding to a removal of 9.01 mg, or 29.3 wt.% of the initial PVDF, which was dissolved and subsequently transported to the collector under $scCO_2$ conditions.

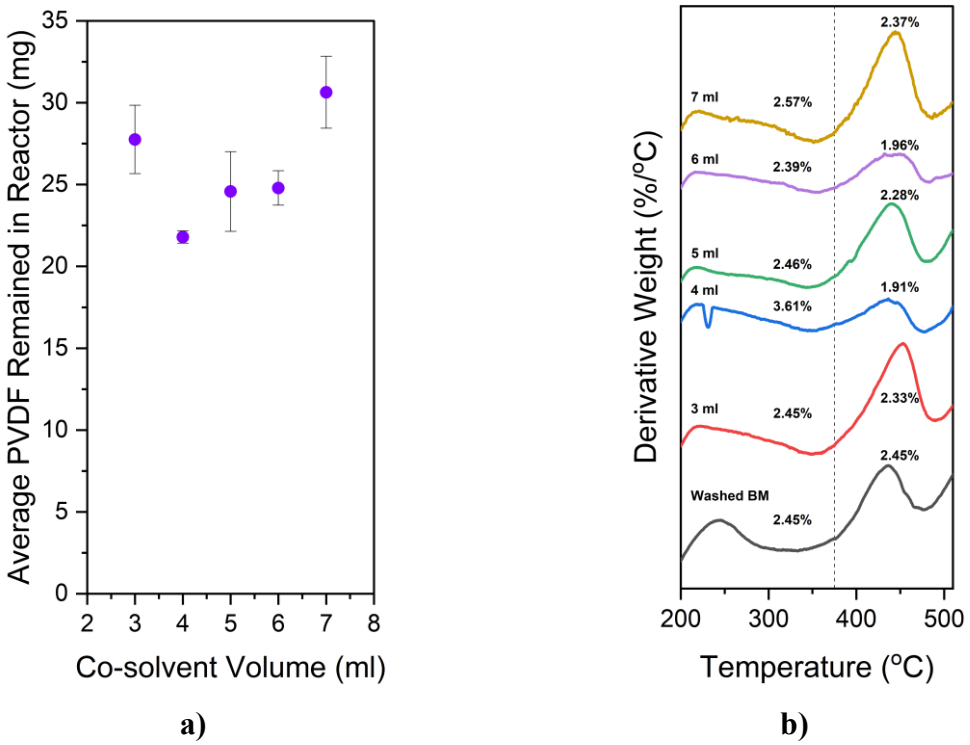

a) **b)**

Figure 7. a) Average PVDF (mg) remained in the BM **b)** DTG (wt.%/°C) of BM remained in the reactor. The dotted line separates region-2 and region-3, and the weight losses of the regions were written as percentages.

A potential explanation for the enhanced recovery of PVDF observed with the use of 4 ml DMSO may be attributed to the mole fraction of CO_2 in the system ($n_{CO2}/(n_{DMSO}+n_{CO2})$), which

was calculated as 0.43, 0.34, 0.26, 0.20, and 0.14 for DMSO volumes of 3, 4, 5, 6, and 7 ml, respectively. Variations in CO_2 mole fraction allow modulation of the DMSO - CO_2 binary phase behavior, as outlined in the phase diagram presented in reference [119]. According to this diagram, increasing the co-solvent volume leads to a reduction in the CO_2 mole fraction within the liquid region (with the exception of the 3 ml case). In this region, a lower co-solvent volume results in higher PVDF dissolution efficiency per unit volume, as illustrated in Figure 8. The liquid phase comprises DMSO containing supercritical CO_2 up to approximately 40 mol% at 70 °C and 80 bar [119,120].

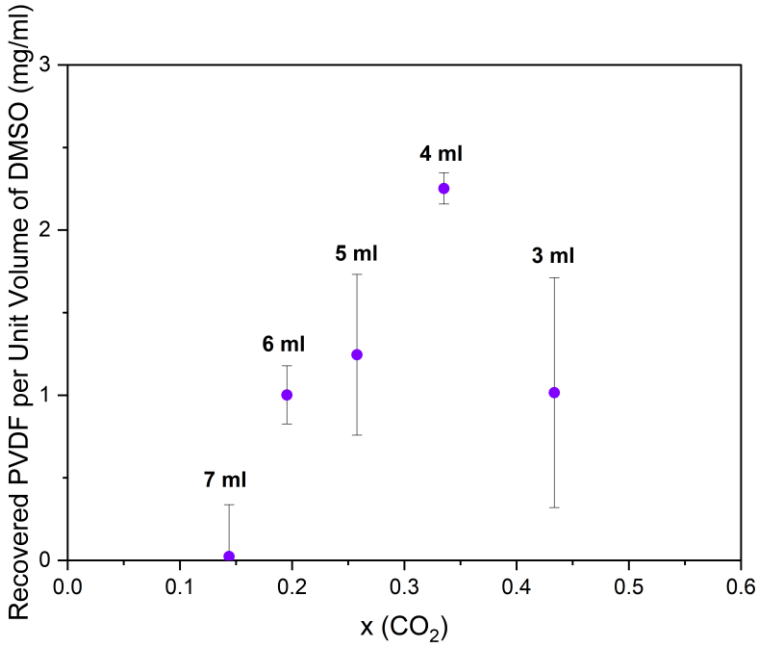

Figure 8. Recovered PVDF per unit volume of co-solvent used (mg/ml) versus mole fraction of CO_2 at 70 °C, 80 bar.

As demonstrated by Ardestani et al. [56], CO_2 acts as an anti-solvent at saturation levels (52 mol% CO_2 at 328 K) in the DMSO–CO_2 system, causing precipitation of solutes dissolved in DMSO. Therefore, as the co-solvent volume decreases, the mole fraction of CO_2 increases, enabling greater PVDF dissolution prior to reaching the saturation limit. This phenomenon may also contribute to the observed decrease in PVDF extraction yield at higher co-solvent volumes. Notably, a distinct drop in the increasing trend was observed at 3 ml DMSO, as shown in Figure 8. At this volume, the system crosses the phase equilibrium line, reaching a CO_2 mole fraction of 0.43 at 80 bar and 70 °C, which corresponds to a biphasic region consisting of liquid (~94 mol% with ~40 mol% CO_2) and supercritical CO_2 (~ 6 mol% with ~99 mol% CO_2).

One plausible explanation is the transition from a single-phase liquid region to a mixed-phase region (liquid + supercritical CO_2). Another contributing factor might be the insufficient co-solvent volume relative to the BM surface area, potentially resulting in DMSO becoming trapped between BM particles, thereby hindering the release and transfer of dissolved PVDF.

It is important to consider that with increasing temperature, the Hildebrand solubility parameter of CO_2 decreases [52], resulting in reduced interactions between $scCO_2$ and DMSO (60.7 $MPa^{1/2}$, [121]). Meantime, elevated temperatures enhance the solubility of PVDF in DMSO [122]. For instance, Yim et al. [53] and Fu et al. [54] achieved extraction yields exceeding 95 wt.% using PVDF powder with DMSO as co-solvent (sample/co-solvent weight ratios of 0.125 and 0.114, respectively) under $scCO_2$ conditions at 70 ℃ and 80 bar. Our findings corroborate the effectiveness of similar parameters for dissolving PVDF from BM. However, BM presents additional complexity due to its heterogeneous particle size distribution and the presence of other organic components, which may also dissolve in the co-solvent.

As reported by Fu et al. [92], the separation of cathode materials from current collectors was investigated using a cathode piece (0.3 g, 1×1 cm) in 4.4 g DMSO, corresponding to a sample/co-solvent weight ratio of 0.068. In this case, 96.7 wt.% liberation efficiency was achieved, yet only 60 wt.% of the PVDF was successfully removed from the cathode. By contrast, our work demonstrated that 29.3 wt.% of the initial PVDF was separated from BM under $scCO_2$ conditions with a sample/co-solvent ratio of 0.227. Further analysis revealed that 26.3 wt.% of the PVDF remained dissolved in DMSO within the reactor, which can be recovered via a PS step.

The PS process was performed using a straightforward protocol. The reactor contents were washed with acetone, allowing the BM to settle for 24 hours, after which the supernatant (a mixture of DMSO and acetone) was decanted. This procedure was repeated twice by adding acetone, and finally BM was dried at 60 ℃, overnight. The BM was subsequently analyzed by TGA, with the results presented in Figure 9. The data indicated that a total of 55.6 wt.% of the initial PVDF was separated from the washed BM.

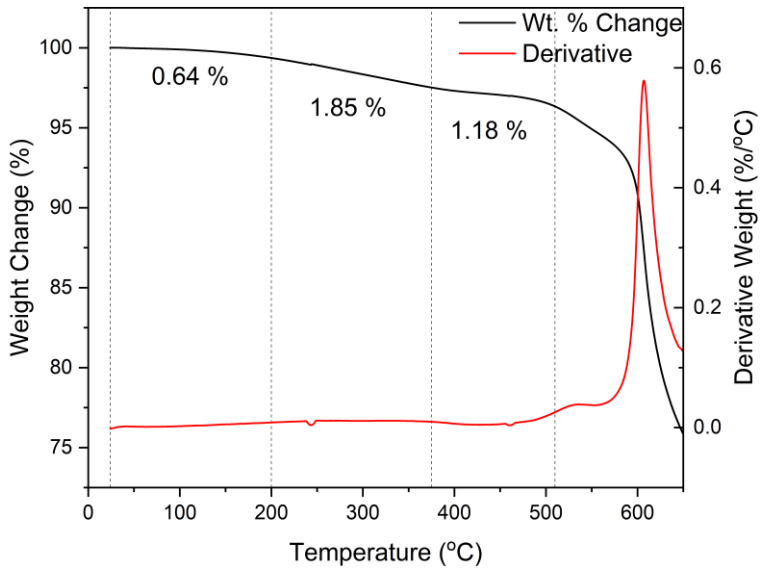

Figure 9. TGA of processed BM with $scCO_2$ and PS process.

The decanted solvent mixture evaporated, and a PVDF film was recovered from the bottom of the vial. This film was further characterized by TGA and XRD. It is noteworthy that the PVDF film obtained from PS, as shown in Figure 10a, contained residual BM particles, which dominated the XRD pattern (Figure 10b). Nevertheless, a minor broad peak at $2\theta \approx 20°$ confirmed the presence of semi-crystalline PVDF. The TGA profile of the film, shown in Figure 11, indicated that PVDF was the predominant component. To obtain purified PVDF, further purification steps, such as filtration, are recommended.

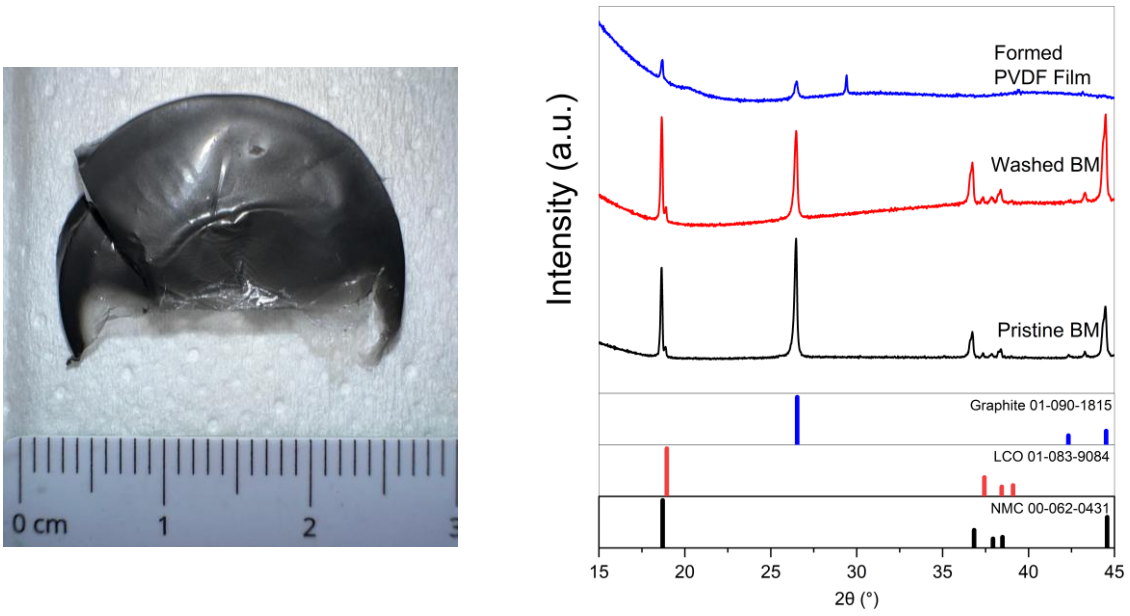

a) **b)**

Figure 10. Recovered PVDF film via PS process **a)** photographic image and **b)** XRD pattern.

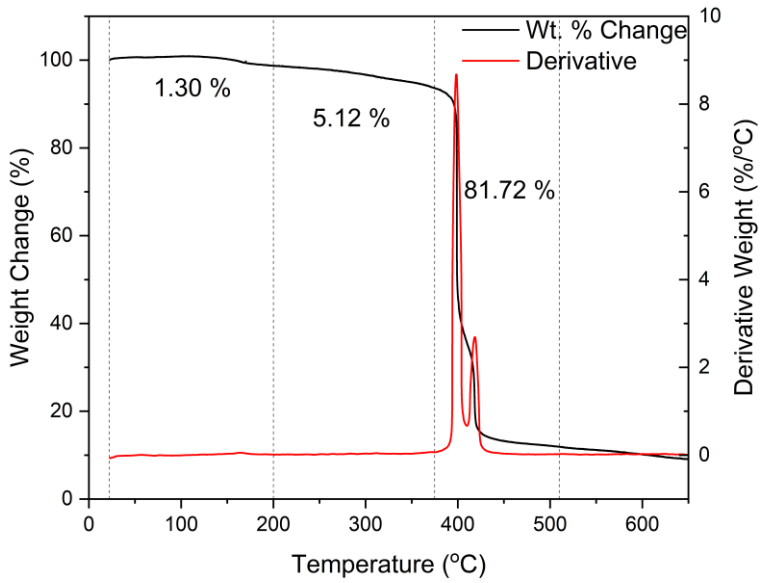

Figure 11. TGA of the recovered PVDF film processed with $scCO_2$ and PS process.

5.5 Further characterization (Paper-I)

Structural and compositional analyses of the pristine-BM, washed-BM, and $scCO_2$-treated BM were conducted using SEM. EDS was applied to three distinct regions of each sample, and average values were calculated with standard deviations. The elemental atomic percentages are presented in Table 2. The results clearly demonstrate the removal of fluorine (F) in the $scCO_2$-treated BM. Fluorine reduction was also observed following the washing process, along with decreases in phosphorus (P) and sulfur (S), suggesting the elimination of $LiPF_6$ and its decomposition products. SEM imaging further revealed a significant reduction in particle size from 93 µm to 43 µm based on measurements of the largest particles using ImageJ software (Figure 12a–f). Fluorine distribution maps are displayed in Figure 12c and d, and the full elemental spectra are provided in Figure 12e and f.

Table 2. EDS results in atomic percentages of BM.

Sample	F	P	S	Mn	Co	Ni
Pristine BM	50.88 (± 2.12)	3.77 (± 0.53)	2.80 (± 0.18)	13.00 (± 1.01)	15.27 (± 2.47)	14.27 (± 0.42)
Washed BM	43.57 (± 1.66)	0.91 (± 0.05)	1.04 (± 0.14)	16.23 (± 0.39)	18.50 (± 1.30)	19.75 (± 0.64)
$scCO_2$ BM	30.38 (± 0.62)	1.07 (± 0.12)	2.02 (± 0.35)	19.73 (± 0.30)	22.71 (± 0.54)	24.11 (± 0.85)

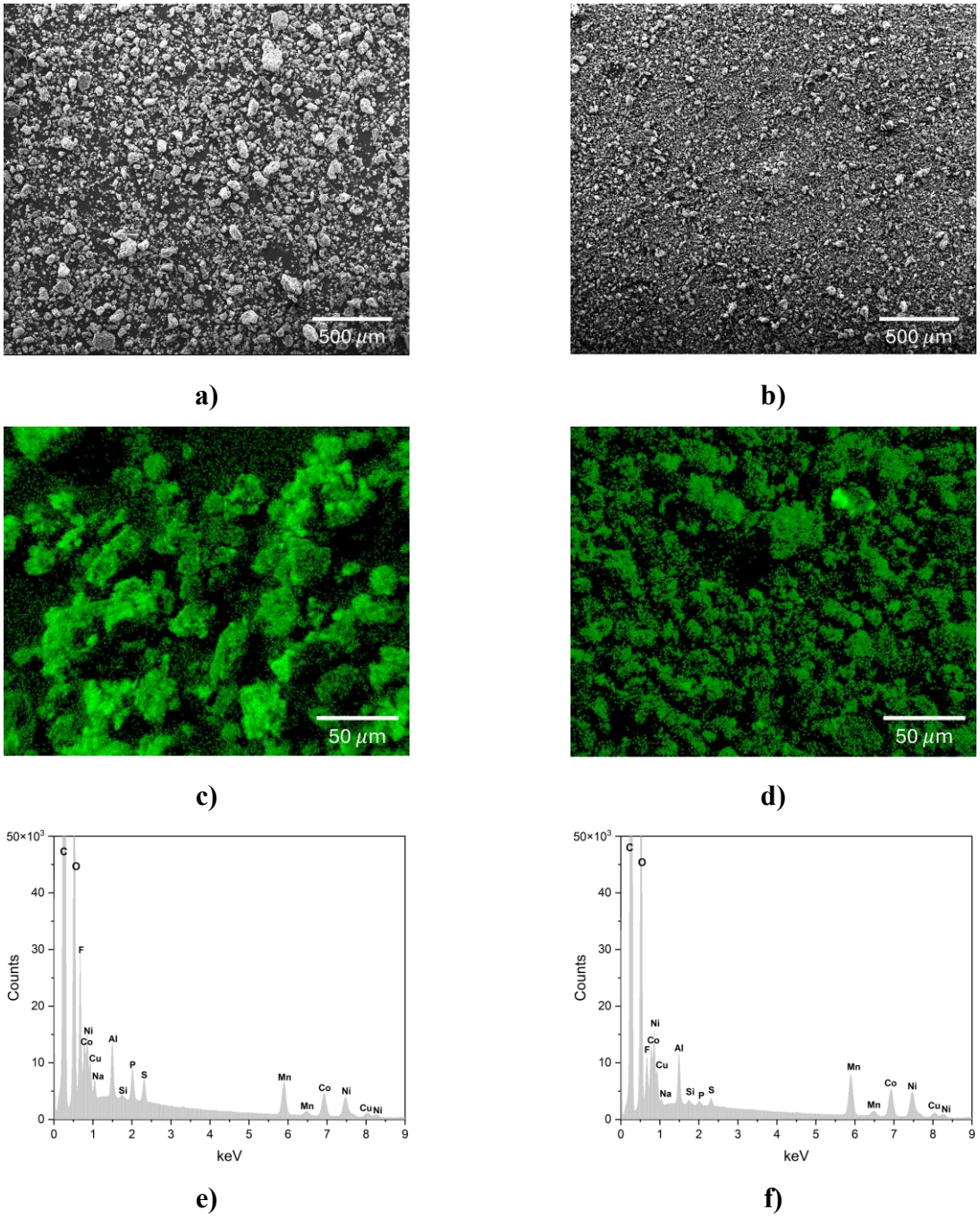

Figure 12. SEM images of **a)** pristine BM and **b)** $scCO_2$-treated BM, EDS F mapping of **c)** pristine and **d)** $scCO_2$-treated BM, EDS spectrum of **e)** pristine BM and **f)** $scCO_2$-treated BM.

The DMSO collected in the glass vial was analyzed by FTIR spectroscopy to confirm the presence of PVDF and to investigate its molecular structure. A 50 µl of the collected DMSO was drop-cast onto aluminum (Al) foil and subsequently dried overnight in an oven at 60°C, resulting in the formation of a PVDF coating on the foil surface. These films were characterized using FTIR spectroscopy, and the spectra are presented in Figure 13. The characteristic vibrational bands corresponding to the α-, β-, and γ-phases of PVDF were identified as

previously reported [117,123–125]. Specifically, the bands located at 883 cm^{-1} (out-of-plane bending vibration of CH_2), 1075 and 1175 cm^{-1} (symmetric stretching of CF_2), and 1408 cm^{-1} (bending vibration of CH_2), marked by vertical dashed lines, are common to all three PVDF phases [37].

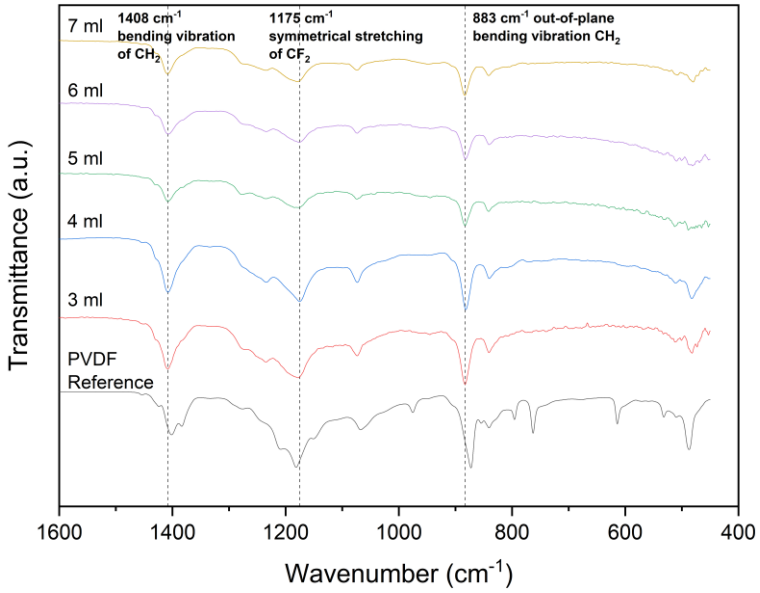

Figure 13. FTIR of PVDF films on Al foil after drying DMSO from the collector.

The spectral data indicate that the recovered PVDF films consist of a mixture of α-, β-, and γ-phases. The phase composition of PVDF is of critical importance in battery applications, with the electroactive β-phase being particularly relevant due to its contribution to the dielectric, piezoelectric, ferroelectric, and pyroelectric properties. In contrast, the α-phase, while thermodynamically stable, is electrically less active. Moreover, the relative phase fractions in PVDF are strongly influenced by the dynamics of solvent evaporation, where drying rate and solvent characteristics play a significant role in determining the final crystalline structure [123,126–129].

XRD analysis was employed to investigate the presence of phases in the BM before and after treatment, and the results are presented in Figure 14. The initial BM composition included $LiNi_{0.3}Mn_{0.3}Co_{0.3}O_2$ (NMC, PDF card no. 00-062-0431), $LiCoO_2$ (LCO, PDF card no. 01-083-9084), and graphite (PDF card no. 00-056-0160). The findings indicate that neither the washing procedure nor the $scCO_2$ treatment altered the primary crystalline phases within the BM. However, peak broadening was observed in the sample collected from filter-1 following the $scCO_2$ process, suggesting potential changes in crystallite size or structural disorder.

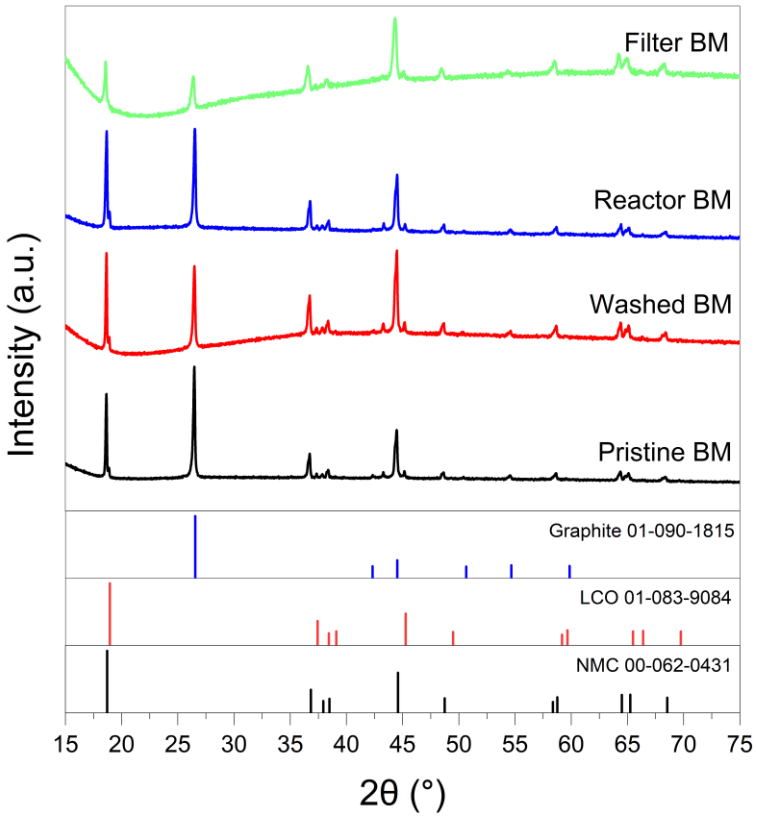

Figure 14. XRD patterns of pristine, washed, recovered (from the reactor), and recovered (from the filter) BM.

The presence of PVDF in the collected DMSO was further verified using ^{19}F NMR spectroscopy. The recorded NMR spectra corresponded well with literature data [130–132], thereby confirming the existence of PVDF in the samples. A characteristic signal observed at −91.1 ppm, as shown in Figure 15, is attributed to the regular head-to-tail (H–T) sequences of –CH_2CF_2–CH_2CF_2– within the polymer chain. In contrast, signals appearing at −113 and −115.3 ppm are associated with head-to-head (H–H, –CH_2CF_2–CF_2CH_2–) and tail-to-tail (T–T, –CF_2CH_2–CH_2CF_2–) linkages, respectively, which are commonly formed as structural defects during polymerization.

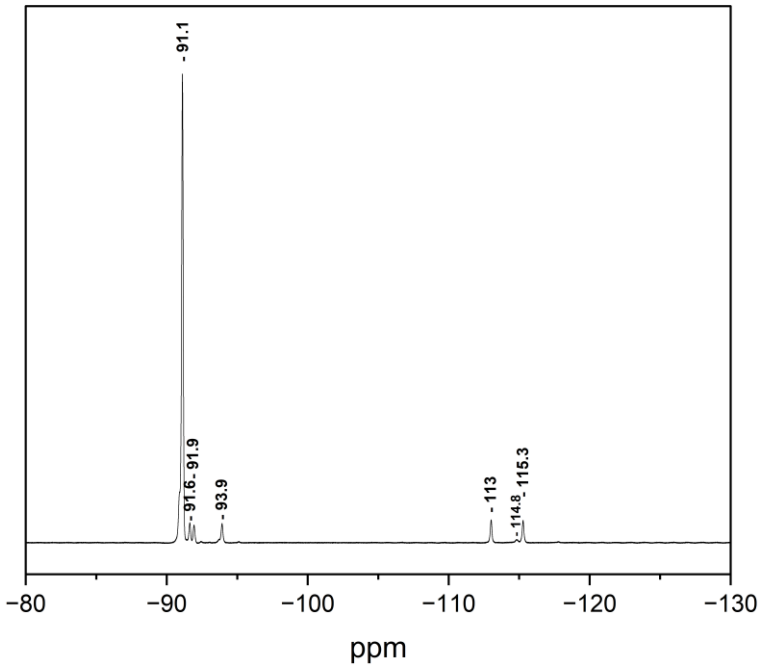

Figure 15. ^{19}F NMR spectrum (600 MHz, DMSO-H6 solvent) of collected DMSO.

The ^{19}F NMR spectrum of the water utilized for washing the BM is presented in Figure 16. Due to the use of water as the solvent medium, the NMR instrument was unable to perform locking and shimming, resulting in a slight deviation in peak positions. Nevertheless, the chemical shifts observed at −72.8 and −74 ppm are characteristic of $LiPF_6$ [133]. These findings indicate that the washing step effectively removed residual Li salt from the pristine BM, in addition to eliminating the CMC binder. This observation is consistent with the outcomes of the elemental analysis and suggests the potential for implementing a sequential recovery approach for battery components prior to the extraction of valuable metals.

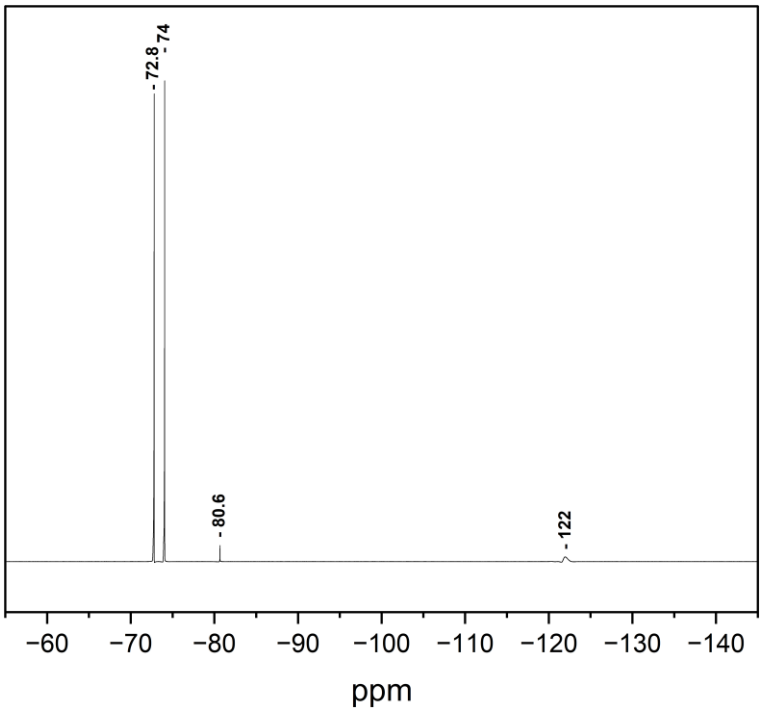

Figure 16. ^{19}F NMR spectrum of washing water after washing the BM.

5.6 PVDF removal at high pressure: pressure scan

The washed BM was processed under $scCO_2$ conditions following the methodology outlined in the experimental section 4.1 and 4.2. 1 g of washed BM and 4 ml of DMSO were introduced into the reactor. Experiments were conducted at 70 °C under pressures of 60, 80, 100, and 120 bar, corresponding to CO_2 mole fractions of 0.25, 0.34, 0.42, and 0.50, respectively. These experimental conditions fall slightly above the 70 °C equilibrium cloud line in the DMSO/CO_2 phase diagram [120]. The objective of the pressure variation study was to determine the favorable operating conditions for co-solvent collection. As the pressure increased from 60 bar to 120 bar, the DMSO collection efficiency rose from 43.3 to 74.6 wt.%. The residual co-solvent remaining in the reactor were 42.5, 54.7, 42.5, and 17.6 wt.% at 60, 80, 100, and 120 bar, respectively.

The residual BM was subsequently utilized to calculate the PVDF recovery yield. PS process of the retained co-solvent was achieved by acetone addition, as described in our previous work [93]. Acetone facilitated the solvent separation by reducing viscosity, and then the remaining solvent was evaporated at 60 °C overnight.

The dried samples were analyzed using TG analysis. The weight loss in the 300 - 430 °C range was used to quantify PVDF removal yield, which is presented in Figure 17a. Figure 17b illustrates the derivative weight change (wt.%/°C) for samples treated at different pressures.

The maximum separation yield, 52.5 wt.% (± 7.1), was observed at 80 bar and 70 °C, corresponding to a CO_2 mole fraction of 0.34.

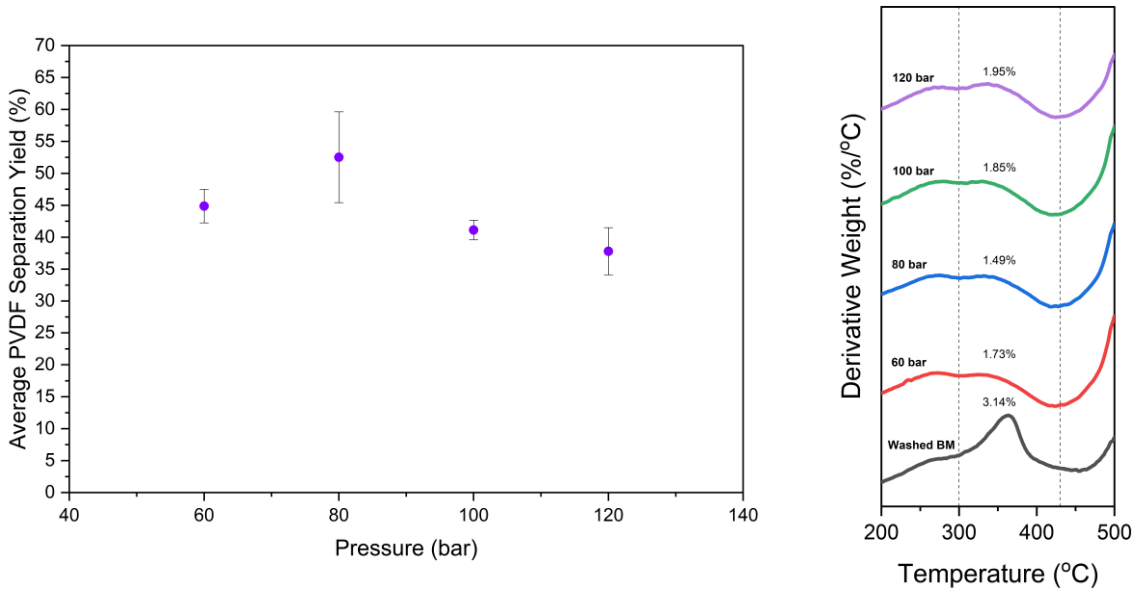

a) **b)**

Figure 17. a) Average separation yield (wt.%), **b)** DTG for processed washed BM in $scCO_2$ and 4 ml of DMSO at 70℃, various pressure, 15 min.

Zahran et al. [120] investigated the excess molar enthalpies (H^E) of the DMSO/CO_2 system at 30 - 60 °C and 90 - 180 bar. Their findings revealed that at constant temperature, a decrease in pressure results in lower H^E values, indicating enhanced solvent-CO_2 interactions. Conversely, at constant pressure, increasing temperature also reduces H^E. Furthermore, at elevated pressures, the temperature effect on enthalpy differences becomes less pronounced. Based on these thermodynamic trends, in our study 80 bar appears to represent the favorable condition for the PVDF - DMSO - CO_2 ternary system at 70 °C with X_{CO_2} = 0.34.

5.7 PVDF removal at high pressure: DMSO:Ac mixture

A complementary series of experiments was carried out at 120 bar and 70 °C for 15 min using a DMSO:acetone (DMSO:Ac) mixture with 1:1 volume ratio and 1 g of washed BM. The pressure of 120 bar was selected to ensure that the solvent-CO_2 mixture remained in the liquid-liquid phase region under all experimental conditions. The CO_2 mole fraction varied by adjusting the co-solvent volume to 3, 4, 5, 6, and 7 ml, corresponding to X_{CO_2} values of 0.62, 0.52, 0.42, 0.34, and 0.26, respectively. The PVDF decomposition range was again observed between 300 and 430 °C. Identical PS and drying procedures were applied to the BM residues.

The average residual co-solvent remaining in the reactor were 11, 15, 6, 11, and 5 wt.% for 3, 4, 5, 6, and 7 ml co-solvent volumes, respectively.

The PVDF removal yields are presented in Figure 18a based on TG analysis, while the derivative TG curves are shown in Figure 18b. The maximum separation yield of 39.5 wt.% was obtained at 120 bar and 70 ℃ with 6 ml of co-solvent (X_{CO_2} = 0.34). This favorable CO_2 mole fraction coincided with that obtained at 80 bar, 70 ℃ using 4 ml of neat DMSO. When compared to the system employing pure DMSO, which achieved a separation yield of 52.5 wt.%, the DMSO:Ac mixture yielded a lower recovery of 39.5 wt.%.

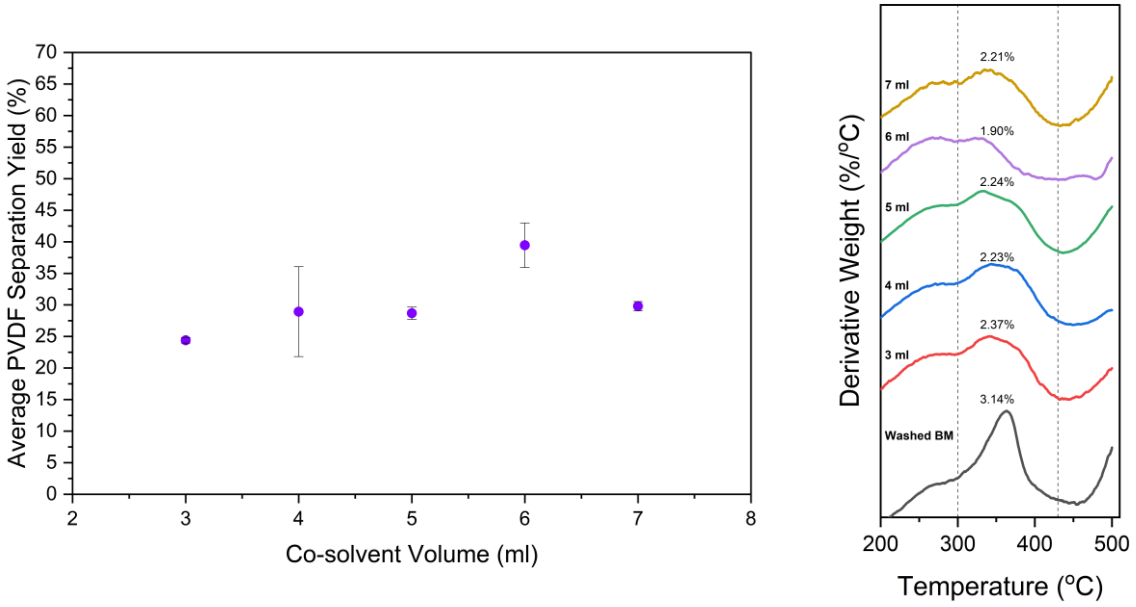

a) **b)**

Figure 18. a) Average separation yield (wt.%), **b)** DTG for processed washed BM in $scCO_2$ and various volume of DMSO:Ac at 70 ℃, 120 bar, 15 min.

The reduction in separation efficiency can be attributed, at least in part, to the increase in pressure from 80 to 120 bar, which approximately doubled the CO_2 density (from ~174 to 345 kg/m^3 at 70 ℃). As a consequence, (i) more CO_2 was dissolved into the liquid phase, (ii) the solvent power of the mixture was diluted, and (iii) the effective Hansen solubility parameter of the ternary system shifted further from that of PVDF. Conversely, acetone is known to dissolve larger quantities of CO_2 than DMSO [134]; therefore, a 1:1 DMSO:Ac mixture may absorb more CO_2 under the same temperature and pressure. This behavior could promote phase separation of the co-solvent into two distinct binary subsystems, namely DMSO-CO_2 and Ac-CO_2, thereby affecting the overall solvation environment and PVDF recovery performance. It is evident that a CO_2 mole fraction of 0.34 represents the favorable condition for achieving the

highest PVDF separation yield in both DMSO and DMSO:Ac systems when operated at 70 °C and 120 bar. Nevertheless, the overall separation efficiency is influenced by pressure, as higher CO_2 densities at elevated pressures tend to reduce PVDF separation yields.

A subsequent series of experiments was conducted using 7 ml of DMSO:Ac under 120 bar for 15 min, while varying the temperature at 30, 50, 70, and 90 °C, corresponding to CO_2 mole fractions of 0.44, 0.36, 0.25, and 0.21, respectively. The purpose of this temperature scan was to increase CO_2 density at lower temperatures, and how it effects the PVDF separation from the BM via enhancing CO_2 dissolution within the co-solvent. The PVDF removal yields and DTG profiles are presented in Figure 19a and b, respectively. The highest separation yield of 45.95 wt.% (± 3.2) was achieved at 90 °C (X_{CO_2} = 0.21). However, a pronounced decline in yield was observed at lower temperatures, reaching 29.80 wt.% (± 0.7), 12.47 wt.% (± 1.3), and 6.55 wt.% (± 0.1) at 70, 50, and 30 °C, respectively. Results suggest that increasing CO_2 density by lowering the temperature is not favorable in terms of PVDF separation from BM.

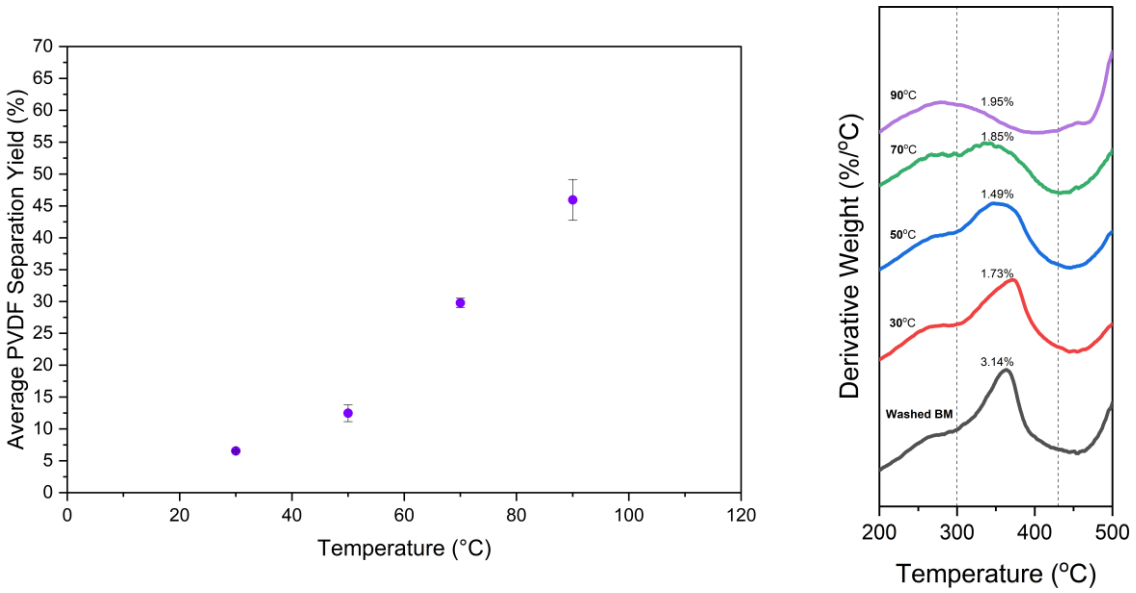

a) **b)**

Figure 19. a) Average separation yield (wt.%), **b)** DTG for processed washed BM in $scCO_2$ and 7 ml of DMSO:Ac at various temperature, 120 bar, 15 min.

One plausible explanation for this trend is that CO_2 exhibits greater solubility in acetone than in DMSO, as previously discussed, which may have induced phase separation of the co-solvent into two distinct binary systems, DMSO / CO_2 and Ac / CO_2. As a result, the original DMSO:Ac / CO_2 mixture, which initially demonstrated favorable Hansen solubility parameter (HSP)

compatibility with PVDF, likely deviated from its favorable solubility region, thereby diminishing PVDF dissolution and extraction efficiency.

An additional contributing factor may be the solid-state nature of PVDF at lower temperatures, which impedes its dissolution. Jiang et al. [59] reported that the melting point of PVDF in acetone is 82.3 °C, whereas the typical melting point of PVDF is approximately 170–180 °C [27,135]. Similarly, Yim et al. [53] and Fu et al. [54] observed that solubility in the $scCO_2$-DMSO system increases with temperature, reaching higher dissolution efficiencies around 70 °C and 60 °C, respectively, at 80 bar.

Jiang et al. [59] reported that the solubility of PVDF in acetone remains below 3 mg/ml at temperatures below 80 °C, but increases substantially with temperature, reaching a maximum of approximately 8 - 10 g/ml at 120 - 150 °C. The solubility behavior was found to be strongly associated with the polymer's melting transition, as solvent presence leads to a depression of the PVDF melting point. The authors suggested that once the temperature exceeds the crystalline melting range, both the dissolution rate and overall solubility of PVDF increase with temperature. Our experimental results are in agreement with this trend, showing that lowering the system temperature results in a corresponding decrease in separation yield. Thus, elevated temperatures enhance PVDF dissolution and consequently improve its separation from the black mass (BM).

To further elucidate this thermal behavior, DSC was performed for pristine PVDF and PVDF dissolved in DMSO (with 1, 25, 50 and 75 wt.%). The corresponding DSC curves are presented in Figure 20. It can be observed that the melting temperature (T_m) of pure PVDF is approximately 164.4 °C, whereas the endothermic peak shifts to 19.3 °C in the presence of DMSO (1 wt.% PVDF). A comparable study involving PVDF and dimethylacetamide (DMAc) exhibited similar results, where the endothermic peak shifted to lower temperatures as the PVDF mass fraction decreased [136]. Specifically, the T_m transitioned from approximately 160 °C to the 60 - 80 °C range as the polymer concentration was reduced, and the melting peak completely disappeared when the PVDF mass fraction reached 23 wt.%. Furthermore, an additional endothermic peak emerged when the PVDF mole fraction was lowered to 52 wt.%. This phenomenon occurs because the solvent acts as a plasticizer for PVDF, thereby decreasing its melting temperature and reducing its degree of crystallinity.

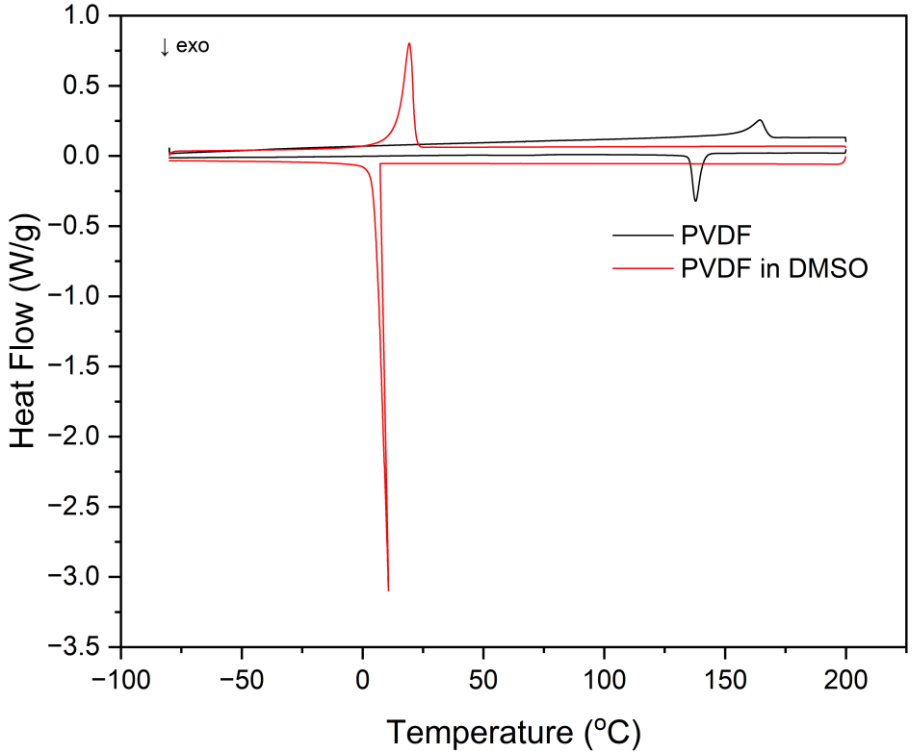

Figure 20. DSC curves of PVDF powder (black) and PVDF powder dissolved in DMSO (red).

To gain deeper insight into the influence of process parameters on PVDF separation, two additional comparative experimental series were conducted employing $scCO_2$ followed by PS treatment. A concise summary of the experimental conditions and corresponding PVDF separation yields is presented in Table 3.

Table 3. Comparison of experimental conditions and PVDF separation yields.

	Co-solvent	**Pressure (bar)**	**Temperature (°C)**	**X_{CO_2}**	**PVDF Separated (wt.%)**
Comparison1	4ml DMSO:Ac	80	70	0.34	35.4
Reference1a	6ml DMSO:Ac	120	70	0.34	39.5
Reference1b	4ml DMSO:Ac	120	70	0.50	28.9
Comparison2	4ml DMSO	80	90	0.30	42.3
Reference2	4ml DMSO	80	70	0.34	52.5

In the first comparison set, a triplicate experiment utilizing 4 ml of a 1:1 DMSO:Ac co-solvent mixture at 80 bar and 70 ℃ (corresponding to a CO_2 mole fraction of 0.34) was compared with a condition employing 6 ml of the same co-solvent at 120 bar and 70 ℃. The obtained PVDF separation efficiency was 35.4 wt.% (± 3.5), which was lower than 39.5 wt.% (± 3.5) that of the reference experiment (6 ml of 1:1 DMSO:Ac at 120 bar and 70 ℃) but higher than the yield 28.9 wt.% (± 7.1) achieved using 4 ml of 1:1 DMSO:Ac at 120 bar and 70 ℃. These observations suggest that a CO_2 mole fraction of 0.34 may represent a favorable region for PVDF separation, while maintaining this fraction at elevated pressures can further enhance the separation yield.

In the second comparative experiment, triplicate trials were conducted using 4 ml of DMSO as the sole co-solvent at 90 ℃ and 80 bar, and the results were compared to those obtained at 70 ℃ under identical pressure and solvent volume. The PVDF separation yield at 90 ℃ was 42.3 wt.% (± 2.0), lower than 52.5 wt.% (± 7.1), the achieved at 70 ℃. This indicates that an increase in temperature does not improve PVDF recovery efficiency when DMSO is used alone, inconsistent with the behavior observed for the 1:1 DMSO:Ac system.

In summary, these results demonstrate that temperature variation has a comparatively minor influence relative to co-solvent composition. The presence of a favorable CO_2 mole fraction appears critical for efficient PVDF separation, while system pressure remains the predominant factor enhancing PVDF recovery from black mass when employing the 1:1 DMSO:Ac co-solvent mixture.

5.8 Further characterization (Paper-II)

For further characterization, three samples were analyzed: the washed BM, the BM processed at 80 bar and 70 ℃ using DMSO as the co-solvent (hereafter referred to as Processed-1), and the BM processed at 120 bar and 70 ℃ with a 1:1 DMSO:Ac co-solvent (hereafter referred to as Processed-2). The DMSO collected in the glass vial, as well as the PVDF films formed during PS, were examined via FTIR spectroscopy to confirm the presence of PVDF and to assess its molecular structure.

Aliquots of 50 µl were extracted from the recovered DMSO and dispensed as droplets onto aluminum foil substrates. The samples were subsequently dried in an oven at 60 ℃ overnight, yielding a thin PVDF coating on the foil surface. Likewise, the DMSO and Ac mixtures from PS were dried to form PVDF films. The resulting films were analyzed using FTIR

spectroscopy, and the corresponding spectra are shown in Figure 21. Recovered PVDF from the collector and PS shows three main phases (α, β, γ) of PVDF.

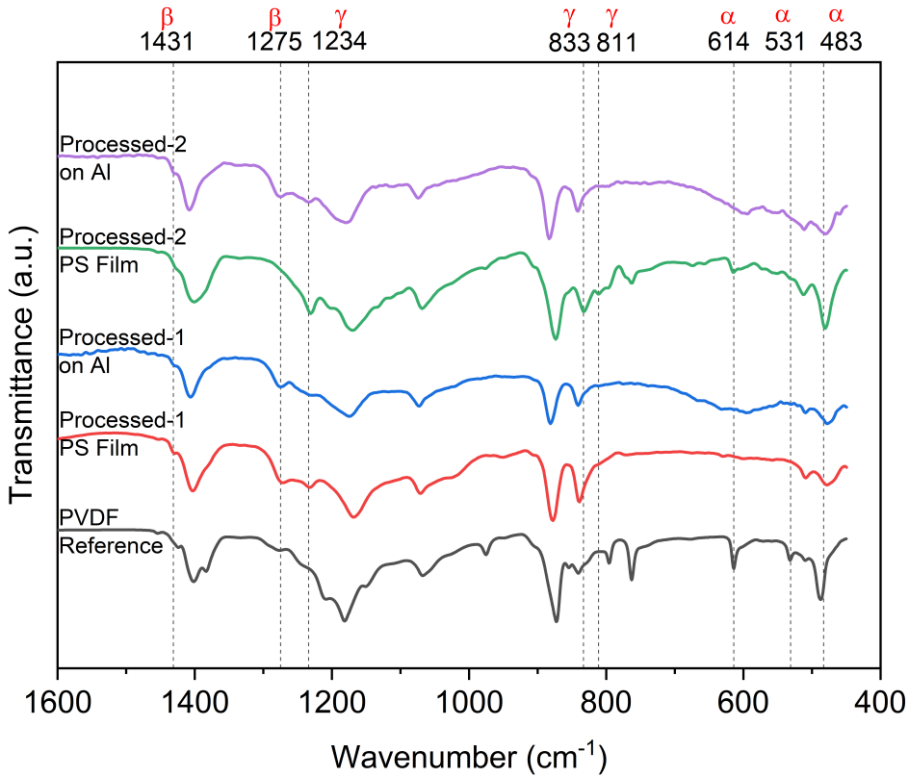

Figure 21. FTIR of pristine and processed PVDF.

The washed BM, Processed-1, and Processed-2 samples were analyzed using SEM to evaluate and compare their morphological features, as presented in Figure 22. The washed BM displayed relatively large agglomerates composed of mixed graphite and cathode active materials. In contrast, the sample from Processed-1 showed a clear liberation of active materials from the graphite matrix, and this separation became even more evident in Processed-2. Although TG analysis indicated that the DMSO-based process removed a greater proportion of PVDF from the BM, the DMSO:Ac treatment produced finer and more uniformly dispersed particles. This refinement suggests that subsequent recovery of valuable metals through leaching could be facilitated by the improved particle morphology.

The same samples were further characterized by EDS for elemental mapping. Three randomly selected regions were analyzed for each sample, and the average atomic percentages are summarized in Table 4 for the washed BM, Processed-1, and Processed-2. A progressive decrease in fluorine content was observed across both processing methods, confirming the removal of PVDF.

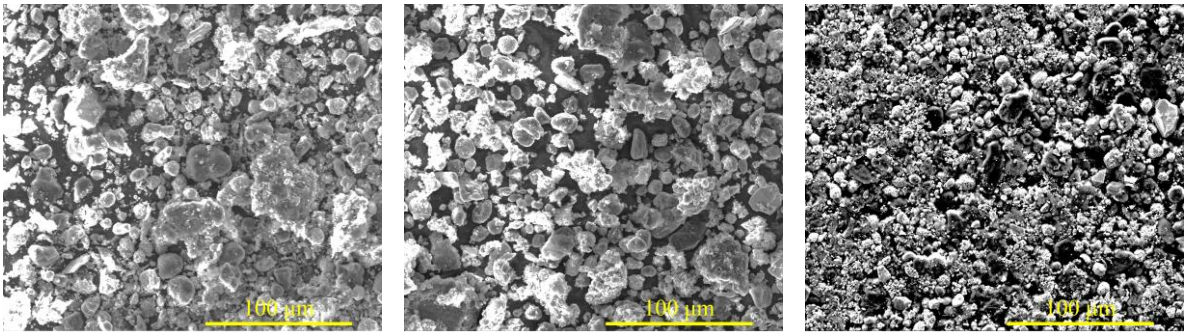

a) **b)** **c)**

Figure 22. SEM images of BM **a)** washed **b)** processed-1 and **c)** processed-2.

Table 4. EDS results in atomic percentages of BM.

	F	**P**	**S**	**Mn**	**Co**	**Ni**
Washed BM	39.77	0.84	1.08	17.01	20.43	20.86
	±1.82	±0.06	±0.14	±0.59	±0.78	±0.64
Processed-1	25.7	0.97	1.22	20.93	25.50	25.68
	± 0.91	± 0.12	± 0.33	± 1.15	± 1.22	± 1.04
Processed-2	31.24	0.85	1.02	20.38	23.32	23.19
	± 2.79	± 0.06	± 0.63	± 0.72	± 1.56	± 0.80

6 Conclusion

In this work, the $scCO_2$ process was employed in combination with DMSO and a 1:1 DMSO:Ac co-solvent system to extract the PVDF binder from industrial BM. The effect of co-solvent composition and volume on recovery yield was systematically investigated. Under favorable conditions, 4 ml DMSO at 70 °C and 80 bar, and 6 ml 1:1 DMSO:Ac at 70 °C and 120 bar (both corresponding to X_{CO_2} = 0.34), cumulative PVDF recovery yields of 55.6 wt.% and 39.5 wt.% were obtained, respectively. When 4 ml DMSO was applied, 1.48 ± 0.52 ml of the co-solvent remained in the reactor containing 8.1 mg of dissolved PVDF, indicating that $scCO_2$ enhanced PVDF solubility in DMSO and significantly shortened the dissolution time compared with atmospheric conditions. Furthermore, PVDF remained solubilized in DMSO even after depressurization to ambient conditions, enabling 29.3 and 26.3 wt.% PVDF separation by $scCO_2$ and post separation processes, respectively. However, PVDF films obtained via post separation required further purification owing to residual BM components (~10 wt.%).

A comparison with conventional dissolution experiments demonstrated that PVDF in BM did not dissolve in DMSO at room temperature even after 18 days, whereas 30.8 wt.% separation occurred at 70 °C under ambient pressure after 24 h. In contrast, complete dissolution was achieved within 15 min under $scCO_2$ conditions, confirming the accelerating effect of CO_2-induced solvent densification. SEM analysis further revealed substantial de-agglomeration of BM particles following PVDF removal, resulting in improved liberation of the cathode active materials and graphite.

A pressure-dependent study using 4 ml DMSO identified 80 bar as a favorable operating point at 70 °C, attributed to the enhanced enthalpic interactions between CO_2 and DMSO. The addition of acetone decreased the viscosity of the co-solvent mixture, thereby improving the co-solvent recovery and limiting the residual fraction within the reactor. When 6 ml of 1:1 DMSO:Ac was used, a maximum PVDF separation yield of 39.5 wt.% was achieved at X_{CO_2} = 0.34, whereas maintaining the same X_{CO_2} at lower pressure resulted in 35.4 wt.% yield. These results indicate 120 bar as a favorable pressure for the DMSO:Ac system. Increasing the process temperature promoted higher PVDF separation for DMSO:Ac mixtures, contrasting with the pure DMSO case, where elevated temperatures did not further enhance dissolution.

Overall, the findings confirm that $scCO_2$ can act as an efficient medium for selective PVDF extraction from industrial BM, offering a rapid, tunable, and environmentally compatible

process compared to conventional solvent-based approaches. The co-solvent composition, system pressure, and CO_2 mole fraction were found to be critical parameters governing both the solubility and recovery efficiency of PVDF.

7 Future Work

The process parameters identified in this study provide a foundation for the design and scale-up of a supercritical CO_2 reactor from milliliter to liter scale. Expanding the system volume to liter would enable the assessment of process reproducibility, solvent dynamics, and CO_2 mass transfer under semi-continuous operation. Such an upscaled setup would also allow for larger batch capacities and improved control over residence time and solvent recovery, facilitating the transition from laboratory-scale experiments toward pilot-scale validation.

The PVDF binder separated under the favorable $scCO_2$ conditions should be subjected to additional purification steps to remove residual inorganic components originating from the black mass. Subsequent physicochemical characterization and electrochemical testing of the purified PVDF in new electrode formulations would verify its reusability and potential performance in next-generation batteries.

Moreover, since PVDF strongly binds the cathode active material and graphite, its removal is expected to significantly enhance the accessibility of the leaching agents during hydrometallurgical treatment. Therefore, a comparative study quantifying the influence of PVDF removal on the leaching efficiency of valuable metals (Li, Co, Ni, Mn) is recommended. Such work would elucidate the synergistic benefits of integrating supercritical CO_2-based PVDF extraction with downstream hydrometallurgical processes, thereby advancing the overall sustainability and resource efficiency of lithium-ion battery recycling.

Acknowledgements

This work was carried out at the Department of Chemistry and Chemical Engineering, Division of Industrial Materials Recycling, Chalmers University of Technology. I would like to express my sincere gratitude to Dr. Burçak Ebin for his supervision, guidance, and continuous encouragement throughout this research. His expertise and thoughtful insights have greatly shaped the direction and quality of this work.

I also wish to extend my appreciation to Dr. Martina Petranikova for her constructive feedback and valuable scientific discussions. My gratitude further goes to all colleagues in the Industrial Materials Recycling group for creating a motivating and supportive research environment.

Special thanks are due to Dr. Shuichi Haraguchi for his technical advice and assistance with DSC characterization.

Financial support from Chalmers University of Technology and the European Union under Grant Agreement No. 101069685 is gratefully acknowledged.

Finally, I dedicate this work to my beloved grandmother, whose memory continues to inspire me every day. Her passing during my studies was deeply painful, and the distance that kept me from attending her funeral remains one of the hardest moments of this journey. This achievement is, in many ways, a tribute to her love, strength, and belief in me. I am also deeply thankful to my parents, sister and friends for their unwavering support, patience, and encouragement throughout this work.

This work was funded by the European Union under Grant Agreement No 101069685. Views and opinions expressed are however those of the author(s) only and do not necessarily reflect those of the European Union or the European Climate, Infrastructure and Environment Executive Agency (CINEA). Neither the European Union nor the granting authority can be held responsible for them.

References

[1] M. Tarascon, JM., Armand, Issues and challenges facing rechargeable lithium batteries, Nature 414 (2001) 359–367. https://doi.org/https://doi.org/10.1038/35104644.

[2] N. Nitta, F. Wu, J.T. Lee, G. Yushin, Li-ion battery materials: Present and future, Materials Today 18 (2015) 252–264. https://doi.org/10.1016/j.mattod.2014.10.040.

[3] G. Harper, R. Sommerville, E. Kendrick, L. Driscoll, P. Slater, R. Stolkin, A. Walton, P. Christensen, O. Heidrich, S. Lambert, A. Abbott, K. Ryder, L. Gaines, P. Anderson, Recycling lithium-ion batteries from electric vehicles, Nature 575 (2019) 75–86. https://doi.org/10.1038/s41586-019-1682-5.

[4] B. Flamme, G. Rodriguez Garcia, M. Weil, M. Haddad, P. Phansavath, V. Ratovelomanana-Vidal, A. Chagnes, Guidelines to design organic electrolytes for lithium-ion batteries: Environmental impact, physicochemical and electrochemical properties, Green Chemistry 19 (2017) 1828–1849. https://doi.org/10.1039/c7gc00252a.

[5] T. Gül, A.F. Pales, E. Connelly, Global EV Outlook 2024 Moving towards increased affordability, Electric Vehicles Intitiative (2024) 79. https://www.iea.org/reports/global-ev-outlook-2024.

[6] F. Degen, M. Winter, D. Bendig, J. Tübke, Energy consumption of current and future production of lithium-ion and post lithium-ion battery cells, Nat Energy 8 (2023) 1284–1295. https://doi.org/10.1038/s41560-023-01355-z.

[7] Z. Lin, T. Liu, X. Ai, C. Liang, Aligning academia and industry for unified battery performance metrics, Nat Commun 9 (2018) 8–12. https://doi.org/10.1038/s41467-018-07599-8.

[8] A. Sobianowska-Turek, W. Urbańska, A. Janicka, M. Zawiślak, J. Matla, The necessity of recycling of waste li-ion batteries used in electric vehicles as objects posing a threat to human health and the environment, Recycling 6 (2021). https://doi.org/10.3390/recycling6020035.

[9] N.P. Lebedeva, L. Boon-Brett, Considerations on the Chemical Toxicity of Contemporary Li-Ion Battery Electrolytes and Their Components, J Electrochem Soc 163 (2016) A821–A830. https://doi.org/10.1149/2.0171606jes.

[10] F. Larsson, P. Andersson, P. Blomqvist, B.E. Mellander, Toxic fluoride gas emissions from lithium-ion battery fires, Sci Rep 7 (2017). https://doi.org/10.1038/s41598-017-09784-z.

[11] P. Andersson, P. Blomqvist, A. Lorén, Investigation of fire emissions from Li-ion batteries Investigation of fire emissions from Li-ion batteries, 2013.

[12] A. Nedjalkov, J. Meyer, M. Köhring, A. Doering, M. Angelmahr, S. Dahle, A. Sander, A. Fischer, W. Schade, Toxic gas emissions from damaged lithium ion batteries-

analysis and safety enhancement solution, Batteries 2 (2016). https://doi.org/10.3390/batteries2010005.

[13] European Parliament, Regulation (EU) 2024/1252 of the European Parliament and of the Council of 11 April 2024 establishing a framework for ensuring a secure and sustainable supply of critical raw materials and amending Regulations (EU) No 168/2013, (EU) 2018/858, (EU) 2018/17, Official Journal of the European Union EN L serie (2024) 1–67. http://data.europa.eu/eli/reg/2024/1252/oj.

[14] Swedish energy agency, Business Finland, innovasjon Norge, Buisness sweden, The Nordic Battery Value Chain-Market drivers, the Nordic value proposition, and decisive market necessities, (2023). https://www.eba250.com/wp-content/uploads/2023/02/NordicBatteryReport.pdf.

[15] E. Commission, EU deal to end sale of new CO2 emitting cars by 2035, European Commission - European Commission (2022). https://ec.europa.eu/commission/presscorner/detail/en/ip_22_6462 (accessed July 8, 2025).

[16] Europäische Union, Directive - 2006/66 - EN - EUR-Lex, (2006) L 266/14. https://eur-lex.europa.eu/legal-content/EN/ALL/?uri=CELEX%3A32006L0066 (accessed July 8, 2025).

[17] European Parliament and the Council of the European Union, Regulation (EU) 2023/1542 of the European Parliament and of the Council of 12 July 2023 concerning batteries and waste batteries, amending Directive 2008/98/EC and Regulation (EU) 2019/1020 and repealing Directive 2006/66/EC, Official Journal of the European Union 66 (2023) 1–117. https://eur-lex.europa.eu/eli/reg/2023/1542/oj/eng.

[18] W. Lv, Z. Wang, H. Cao, Y. Sun, Y. Zhang, Z. Sun, A Critical Review and Analysis on the Recycling of Spent Lithium-Ion Batteries, ACS Sustain Chem Eng 6 (2018) 1504–1521. https://doi.org/10.1021/acssuschemeng.7b03811.

[19] M.C. Etude, A.I. Ikeuba, C.N. Njoku, E. Yakubu, H.C. Uzoma, C.E. Mgbemere, D.I. Udunwa, Recycling lithium-ion batteries: A review of current status and future directions, Sustainable Chemistry One World 4 (2024) 100027. https://doi.org/10.1016/j.scowo.2024.100027.

[20] P. Cattaneo, D. Callegari, D. Merli, C. Tealdi, D. Vadivel, C. Milanese, V. Kapelyushko, F. D'Aprile, E. Quartarone, Sorting, Characterization, Environmentally Friendly Recycling, and Reuse of Components from End-of-Life 18650 Li Ion Batteries, Adv Sustain Syst 7 (2023) 1–27. https://doi.org/10.1002/adsu.202300161.

[21] J. Wesselkämper, L. Dahrendorf, L. Mauler, S. Lux, S. von Delft, Towards circular battery supply chains: Strategies to reduce material demand and the impact on mining and recycling, Resources Policy 95 (2024). https://doi.org/10.1016/j.resourpol.2024.105160.

[22] J. Neumann, M. Petranikova, M. Meeus, J.D. Gamarra, R. Younesi, M. Winter, S. Nowak, Recycling of Lithium-Ion Batteries—Current State of the Art, Circular Economy, and Next Generation Recycling, Adv Energy Mater 12 (2022). https://doi.org/10.1002/aenm.202102917.

[23] C. Ekberg, M. Petranikova, Lithium Batteries Recycling, Elsevier Inc., 2015. https://doi.org/10.1016/B978-0-12-801417-2.00007-4.

[24] S. Balachandran, K. Forsberg, T. Lemaître, N. Vieceli, G. Lombardo, M. Petranikova, Comparative study for selective lithium recovery via chemical transformations during incineration and dynamic pyrolysis of EV li-ion batteries, Metals (Basel) 11 (2021). https://doi.org/10.3390/met11081240.

[25] N. Sharmili, R. Nagi, P. Wang, A review of research in the Li-ion battery production and reverse supply chains, J Energy Storage 68 (2023) 107622. https://doi.org/10.1016/j.est.2023.107622.

[26] B. Wang, Y. Yin, H. Deng, H. Zhu, G. Li, W. He, Migration, transformation, and management of fluorine-containing substances in lithium-ion batteries during recycling − A review, Sep Purif Technol 358 (2025) 130283. https://doi.org/10.1016/j.seppur.2024.130283.

[27] M. Wang, K. Liu, J. Yu, Q. Zhang, Y. Zhang, M. Valix, D.C.W. Tsang, Challenges in Recycling Spent Lithium-Ion Batteries: Spotlight on Polyvinylidene Fluoride Removal, Global Challenges 7 (2023). https://doi.org/10.1002/gch2.202200237.

[28] Y. Ji, C.T. Jafvert, N.N. Zyaykina, F. Zhao, Decomposition of PVDF to delaminate cathode materials from end-of-life lithium-ion battery cathodes, J Clean Prod 367 (2022). https://doi.org/10.1016/j.jclepro.2022.133112.

[29] R. Golmohammadzadeh, Z. Dimachki, W. Bryant, J. Zhang, P. Biniaz, M. M Banaszak Holl, C. Pozo-Gonzalo, P. Chakraborty Banerjee, Removal of polyvinylidene fluoride binder and other organics for enhancing the leaching efficiency of lithium and cobalt from black mass, J Environ Manage 343 (2023) 118205. https://doi.org/10.1016/j.jenvman.2023.118205.

[30] H. Wang, J. Liu, X. Bai, S. Wang, D. Yang, Y. Fu, Y. He, Separation of the cathode materials from the Al foil in spent lithium-ion batteries by cryogenic grinding, Waste Management 91 (2019) 89–98. https://doi.org/10.1016/j.wasman.2019.04.058.

[31] J. Liu, X. Bai, J. Hao, H. Wang, T. Zhang, X. Tang, S. Wang, Y. He, Efficient liberation of electrode materials in spent lithium-ion batteries using a cryogenic ball mill, J Environ Chem Eng 9 (2021) 106017. https://doi.org/10.1016/j.jece.2021.106017.

[32] C. Tokoro, S. Lim, K. Teruya, M. Kondo, K. Mochidzuki, T. Namihira, Y. Kikuchi, Separation of cathode particles and aluminum current foil in Lithium-Ion battery by high-voltage pulsed discharge Part I: Experimental investigation, Waste Management 125 (2021) 58–66. https://doi.org/10.1016/j.wasman.2021.01.008.

[33] G. Zhang, Y. He, Y. Feng, H. Wang, X. Zhu, Pyrolysis-Ultrasonic-Assisted Flotation Technology for Recovering Graphite and LiCoO2 from Spent Lithium-Ion Batteries, ACS Sustain Chem Eng 6 (2018) 10896–10904. https://doi.org/10.1021/acssuschemeng.8b02186.

[34] C. Hanisch, T. Loellhoeffel, J. Diekmann, K.J. Markley, W. Haselrieder, A. Kwade, Recycling of lithium-ion batteries: A novel method to separate coating and foil of electrodes, J Clean Prod 108 (2015) 301–311. https://doi.org/10.1016/j.jclepro.2015.08.026.

[35] L. Sun, K. Qiu, Vacuum pyrolysis and hydrometallurgical process for the recovery of valuable metals from spent lithium-ion batteries, J Hazard Mater 194 (2011) 378–384. https://doi.org/10.1016/j.jhazmat.2011.07.114.

[36] Y. Bai, R. Essehli, C.J. Jafta, K.M. Livingston, I. Belharouak, Recovery of Cathode Materials and Aluminum Foil Using a Green Solvent, ACS Sustain Chem Eng 9 (2021) 6048–6055. https://doi.org/10.1021/acssuschemeng.1c01293.

[37] Y. Bai, N. Muralidharan, J. Li, R. Essehli, I. Belharouak, Sustainable Direct Recycling of Lithium-Ion Batteries via Solvent Recovery of Electrode Materials, ChemSusChem 13 (2020) 5664–5670. https://doi.org/10.1002/cssc.202001479.

[38] O. Buken, K. Mancini, A. Sarkar, A sustainable approach to cathode delamination using a green solvent, RSC Adv 11 (2021) 27356–27368. https://doi.org/10.1039/d1ra04922d.

[39] X. Zeng, J. Li, Innovative application of ionic liquid to separate Al and cathode materials from spent high-power lithium-ion batteries, J Hazard Mater 271 (2014) 50–56. https://doi.org/10.1016/j.jhazmat.2014.02.001.

[40] M. Wang, Q. Tan, L. Liu, J. Li, Efficient Separation of Aluminum Foil and Cathode Materials from Spent Lithium-Ion Batteries Using a Low-Temperature Molten Salt, ACS Sustain Chem Eng 7 (2019) 8287–8294. https://doi.org/10.1021/acssuschemeng.8b06694.

[41] Y. Hua, Z. Xu, B. Zhao, Z. Zhang, Efficient separation of electrode active materials and current collector metal foils from spent lithium-ion batteries by a green deep eutectic solvent, Green Chemistry 24 (2022) 8131–8141. https://doi.org/10.1039/d2gc02844a.

[42] Y. Ji, C.T. Jafvert, N.N. Zyaykina, F. Zhao, Decomposition of PVDF to delaminate cathode materials from end-of-life lithium-ion battery cathodes, J Clean Prod 367 (2022). https://doi.org/10.1016/j.jclepro.2022.133112.

[43] A.G. Veiga, F.G. de A. Dias, L. do N. Batista, M.L.M. Rocco, M.F. Costa, Reprocessed poly(vinylidene fluoride): A comparative approach for mechanical recycling purposes, Mater Today Commun 25 (2020) 101269. https://doi.org/10.1016/j.mtcomm.2020.101269.

[44] Y. Bai, R. Essehli, C.J. Jafta, K.M. Livingston, I. Belharouak, Recovery of Cathode Materials and Aluminum Foil Using a Green Solvent, ACS Sustain Chem Eng 9 (2021) 6048–6055. https://doi.org/10.1021/acssuschemeng.1c01293.

[45] O. Buken, K. Mancini, A. Sarkar, A sustainable approach to cathode delamination using a green solvent, RSC Adv 11 (2021) 27356–27368. https://doi.org/10.1039/d1ra04922d.

[46] A. Sarkar, R. May, S. Ramesh, W. Chang, L.E. Marbella, Recovery and Reuse of Composite Cathode Binder in Lithium Ion Batteries, ChemistryOpen 10 (2021) 545–552. https://doi.org/10.1002/open.202100060.

[47] X. Zhong, J. Han, L. Chen, W. Liu, F. Jiao, H. Zhu, W. Qin, Binding mechanisms of PVDF in lithium ion batteries, Appl Surf Sci 553 (2021) 149564. https://doi.org/10.1016/j.apsusc.2021.149564.

[48] A. Sarkar, R. May, S. Ramesh, W. Chang, L.E. Marbella, Recovery and Reuse of Composite Cathode Binder in Lithium Ion Batteries, ChemistryOpen 10 (2021) 545–552. https://doi.org/10.1002/open.202100060.

[49] M. Sihvonen, E. Järvenpää, V. Hietaniemi, R. Huopalahti, Advances in supercritical carbon dioxide technologies, Trends Food Sci Technol 10 (1999) 217–222. https://doi.org/10.1016/S0924-2244(99)00049-7.

[50] P. Nikolai, B. Rabiyat, A. Aslan, A. Ilmutdin, Supercritical CO2: Properties and Technological Applications-A Review, 2019. https://doi.org/10.1007/s11630-019-1118-4.

[51] F. Rindfleisch, T.P. DiNoia, M.A. McHugh, Solubility of polymers and copolymers in supercritical CO2, Journal of Physical Chemistry 100 (1996) 15581–15587. https://doi.org/10.1021/jp9615823.

[52] P. Cattaneo, F. D'Aprile, V. Kapelyushko, P. Mustarelli, E. Quartarone, Supercritical CO2 technology for the treatment of end-of-life lithium-ion batteries, RSC Sustainability 2 (2024) 1692–1707. https://doi.org/10.1039/d4su00044g.

[53] J.H. Yim, W.W. Seo, J. Sik Jeon, J. Sung Lim, J. won Lee, Extraction of polyvinylidene fluoride binder materials for used secondary batteries using supercritical CO2 for an effective battery recycling process, Journal of Industrial and Engineering Chemistry (2024). https://doi.org/10.1016/j.jiec.2024.09.030.

[54] Y. Fu, J. Schuster, M. Petranikova, B. Ebin, Innovative recycling of organic binders from electric vehicle lithium-ion batteries by supercritical carbon dioxide extraction, Resour Conserv Recycl 172 (2021). https://doi.org/10.1016/j.resconrec.2021.105666.

[55] N. Hayagan, C. AYMONIER, L. Croguennec, C. Faure, J.-B. Ledeuil, M. Morcrette, R. Dedryvère, J. OLCHOWKA, G. Philippot, Direct recycling process using pressurized CO2 for Li-ion batteries positive electrode production scraps, SSRN Electronic Journal (2024). https://doi.org/10.2139/ssrn.4735734.

[56] N. Saadati Ardestani, M. Amani, A numerical approach to determine the optimal condition of the gas anti-solvent supercritical process for nanoparticles production, Sci Rep 12 (2022) 1–15. https://doi.org/10.1038/s41598-022-15754-x.

[57] J.E. Marshall, A. Zhenova, S. Roberts, T. Petchey, P. Zhu, C.E.J. Dancer, C.R. McElroy, E. Kendrick, V. Goodship, On the solubility and stability of polyvinylidene fluoride, Polymers (Basel) 13 (2021) 1–31. https://doi.org/10.3390/polym13091354.

[58] A. Kordikowski, A.P. Schenk, R.M. Van Nielen, C.J. Peters, Volume expansions and vapor-liquid equilibria of binary mixtures of a variety of polar solvents and certain near-critical solvents, J Supercrit Fluids 8 (1995) 205–216. https://doi.org/10.1016/0896-8446(95)90033-0.

[59] G. Jiang, D. Lee, D. Raimbault, P.A. Anderson, G.A. Leeke, Acetone as an agent for PVDF recovery and delamination of lithium-ion battery electrodes, Resour Conserv Recycl 209 (2024) 107778. https://doi.org/10.1016/j.resconrec.2024.107778.

[60] J.M.O. Bacicheti, J.A. Oliveira, T.V. Barros, L. Ferreira-Pinto, P.F.A. Castillo, V.F. Cabral, L. Cardozo-Filho, Phase Equilibria of {Carbon Dioxide + Acetone + Dimethyl Sulfoxide} Systems: Experimental Data and Thermodynamic Modeling, J Solution Chem 51 (2022) 1292–1309. https://doi.org/10.1007/s10953-022-01196-6.

[61] A. Bottino, G. Capannelli, S. Munari, A. Turturro, Solubility parameters of poly(vinylidene fluoride), J Polym Sci B Polym Phys 26 (1988) 785–794. https://doi.org/10.1002/polb.1988.090260405.

[62] M. Lora, J.S. Lim, M.A. McHugh, Comparison of the solubility of PVF and PVDF in supercritical CH2F2 and CO2 and in CO2 with acetone, dimethyl ether, and ethanol, Journal of Physical Chemistry B 103 (1999) 2818–2822. https://doi.org/10.1021/jp9844462.

[63] F.S. Tekin, P.Z. Çulfaz-Emecen, Controlling Cellulose Membrane Performance via Solvent Choice during Precursor Membrane Formation, ACS Appl Polym Mater 5 (2023) 2185–2194. https://doi.org/10.1021/acsapm.2c02185.

[64] D.L. Thompson, J.M. Hartley, S.M. Lambert, M. Shiref, G.D.J. Harper, E. Kendrick, P. Anderson, K.S. Ryder, L. Gaines, A.P. Abbott, The importance of design in lithium ion battery recycling-a critical review, Green Chemistry 22 (2020) 7585–7603. https://doi.org/10.1039/d0gc02745f.

[65] H.C. Chen, S.S. Li, S.L. Wu, C.Y. Lee, Design of a modular battery management system for electric motorcycle, Energies (Basel) 14 (2021) 1–16. https://doi.org/10.3390/en14123532.

[66] F. Hashemniya, A. Balachandran, E. Frisk, M. Krysander, Structural Diagnosability Analysis of Switched and Modular Battery Packs, in: Proceedings - 2024 Prognostics and System Health Management Conference, PHM 2024, 2024: pp. 362–369. https://doi.org/10.1109/PHM61473.2024.00070.

[67] D.N. Hummes, J. Hunt, B.B. Hervé, P.S. Schneider, P.M. Montanari, A comparative study of different battery geometries used in electric vehicles, Latin American Journal of Energy Research 10 (2023) 94–114. https://doi.org/10.21712/lajer.2023.v10.n2.p94-114.

[68] F. Schipper, D. Aurbach, A brief review: Past, present and future of lithium ion batteries, Russian Journal of Electrochemistry 52 (2016) 1095–1121. https://doi.org/10.1134/S1023193516120120.

[69] C. Peschel, S. van Wickeren, Y. Preibisch, V. Naber, D. Werner, L. Frankenstein, F. Horsthemke, U. Peuker, M. Winter, S. Nowak, Comprehensive Characterization of Shredded Lithium-Ion Battery Recycling Material, Chemistry - A European Journal 28 (2022). https://doi.org/10.1002/chem.202200485.

[70] J. Choi, P.J. Kim, A roadmap of battery separator development: Past and future, Curr Opin Electrochem 31 (2022) 100858. https://doi.org/10.1016/j.coelec.2021.100858.

[71] F. Gebert, M. Longhini, F. Conti, A.J. Naylor, An electrochemical evaluation of state-of-the-art non-flammable liquid electrolytes for high-voltage lithium-ion batteries, J Power Sources 556 (2023). https://doi.org/10.1016/j.jpowsour.2022.232412.

[72] M. Pigłowska, B. Kurc, M. Galiński, P. Fuć, M. Kamińska, N. Szymlet, P. Daszkiewicz, Challenges for safe electrolytes applied in lithium-ion cells—a review, Materials 14 (2021). https://doi.org/10.3390/ma14226783.

[73] G.A. Giffin, The role of concentration in electrolyte solutions for non-aqueous lithium-based batteries, Nat Commun 13 (2022). https://doi.org/10.1038/s41467-022-32794-z.

[74] Q. He, J. Ning, H. Chen, Z. Jiang, J. Wang, D. Chen, C. Zhao, Z. Liu, I.F. Perepichka, H. Meng, W. Huang, Achievements, challenges, and perspectives in the design of polymer binders for advanced lithium-ion batteries, Chem Soc Rev 53 (2024) 7091–7157. https://doi.org/10.1039/d4cs00366g.

[75] C.M. Costa, E. Lizundia, S. Lanceros-Méndez, Polymers for advanced lithium-ion batteries: State of the art and future needs on polymers for the different battery components, Prog Energy Combust Sci 79 (2020). https://doi.org/10.1016/j.pecs.2020.100846.

[76] H. Chen, M. Ling, L. Hencz, H.Y. Ling, G. Li, Z. Lin, G. Liu, S. Zhang, Exploring Chemical, Mechanical, and Electrical Functionalities of Binders for Advanced Energy-Storage Devices, Chem Rev 118 (2018) 8936–8982. https://doi.org/10.1021/acs.chemrev.8b00241.

[77] P. Siwak, V. Leshchynsky, E. Strumban, M. Pantea, D. Garbiec, R. Maev, The CaO Enhanced Defluorination and Air-Jet Separation of Cathode-Active Material Coating for Direct Recycling Li-Ion Battery Electrodes, Metals (Basel) 14 (2024). https://doi.org/10.3390/met14121466.

[78] P. Liu, X. Mi, H. Zhao, L. Cai, F. Luo, C. Liu, Z. Wang, C. Deng, J. He, G. Zeng, X. Luo, Effects of incineration and pyrolysis on removal of organics and liberation of cathode active materials derived from spent ternary lithium-ion batteries, Waste Management 169 (2023) 342–350. https://doi.org/10.1016/j.wasman.2023.07.025.

[79] H. Isozumi, T. Horiba, K. Kubota, K. Hida, T. Matsuyama, S. Yasuno, S. Komaba, Application of modified styrene-butadiene-rubber-based latex binder to high-voltage operating LiCoO2 composite electrodes for lithium-ion batteries, J Power Sources 468 (2020). https://doi.org/10.1016/j.jpowsour.2020.228332.

[80] J.H. Park, S.H. Kim, K.H. Ahn, Role of carboxymethyl cellulose binder and its effect on the preparation process of anode slurries for Li-ion batteries, Colloids Surf A Physicochem Eng Asp 664 (2023). https://doi.org/10.1016/j.colsurfa.2023.131130.

[81] C. Cui, X. Tang, J. Wang, R. Cheng, C. Zhang, X. Wang, Nanostructured Super P Carbon Black for Lithium Storage: Understanding toward the Mechanism, ACS Appl Nano Mater 8 (2025) 9349–9355. https://doi.org/10.1021/acsanm.5c00944.

[82] Y. Zhang, S. Lu, F. Lou, Z. Yu, Leveraging Synergies by Combining Polytetrafluorethylene with Polyvinylidene Fluoride for Solvent-Free Graphite Anode Fabrication, Energy Technology 10 (2022). https://doi.org/10.1002/ente.202200732.

[83] F. Sun, D.R. Wheeler, The Effects of Lithium Ions and pH on the Function of Polyacrylic Acid Binder for Silicon Anodes, J Electrochem Soc 170 (2023) 080502. https://doi.org/10.1149/1945-7111/aceab1.

[84] P.M. Tembo, C. Dyer, V. Subramanian, Lithium-ion battery recycling—a review of the material supply and policy infrastructure, NPG Asia Mater 16 (2024). https://doi.org/10.1038/s41427-024-00562-8.

[85] M. Rinne, H. Lappalainen, M. Lundström, Evaluating the possibilities and limitations of the pyrometallurgical recycling of waste Li-ion batteries using simulation and life cycle assessment, Green Chemistry 27 (2025) 2522–2537. https://doi.org/10.1039/d4gc05409a.

[86] J. Furlanetto, M.V.C. de Lara, M. Simionato, V. do Nascimento, G.D. Telli, An Overview of Lithium-Ion Battery Recycling: A Comparison of Brazilian and International Scenarios, World Electric Vehicle Journal 16 (2025). https://doi.org/10.3390/wevj16070371.

[87] S. Xiaodong, V. Ishchenko, Environmental Impact Analysis of Waste Lithium-Ion Battery Cathode Recycling, Journal of Ecological Engineering 25 (2024) 352–358. https://doi.org/10.12911/22998993/189187.

[88] M. Müller, H.E. Obuz, S. Keber, F. Tekmanli, L.N. Mettke, B. Yagmurlu, Concepts for the Sustainable Hydrometallurgical Processing of End-of-Life Lithium Iron Phosphate (LFP) Batteries, Sustainability (Switzerland) 16 (2024). https://doi.org/10.3390/su162411267.

[89] G. Lombardo, B. Ebin, M.R. Mark, B.M. Steenari, M. Petranikova, Incineration of EV Lithium-ion batteries as a pretreatment for recycling – Determination of the potential formation of hazardous by-products and effects on metal compounds, J Hazard Mater 393 (2020). https://doi.org/10.1016/j.jhazmat.2020.122372.

[90] M. Petranikova, P.L. Naharro, N. Vieceli, G. Lombardo, B. Ebin, Recovery of critical metals from EV batteries via thermal treatment and leaching with sulphuric acid at ambient temperature, Waste Management 140 (2022) 164–172. https://doi.org/10.1016/j.wasman.2021.11.030.

[91] J. Sharma, C. Totee, V. Kulshrestha, B. Ameduri, Spectroscopic evidence and mechanistic insights on dehydrofluorination of PVDF in alkaline medium, Eur Polym J 201 (2023) 112580. https://doi.org/10.1016/j.eurpolymj.2023.112580.

[92] Y. Fu, X. Dong, B. Ebin, Resource Recovery of Spent Lithium-Ion Battery Cathode Materials by a Supercritical Carbon Dioxide System, Molecules 29 (2024) 1–13. https://doi.org/10.3390/molecules29071638.

[93] Y. Akbaş, M. Petranikova, B. Ebin, Co-solvent controlled PVDF extraction from spent Li-ion batteries using supercritical CO2, Sep Purif Technol 376 (2025). https://doi.org/10.1016/j.seppur.2025.134056.

[94] B. Subramaniam, R.A. Rajewski, K. Snavely, Pharmaceutical processing with supercritical carbon dioxide, J Pharm Sci 86 (1997) 885–890. https://doi.org/10.1021/js9700661.

[95] C. Aymonier, A. Loppinet-Serani, H. Reverón, Y. Garrabos, F. Cansell, Review of supercritical fluids in inorganic materials science, Journal of Supercritical Fluids 38 (2006) 242–251. https://doi.org/10.1016/j.supflu.2006.03.019.

[96] M.L. Campbell, D.L. Apodaca, M.Z. Yates, T.M. McCleskey, E.R. Birnbaum, Metal extraction from heterogeneous surfaces using carbon dioxide microemulsions, Langmuir 17 (2001) 5458–5463. https://doi.org/10.1021/la0104166.

[97] H. Ohde, J.M. Rodriguez, X.R. Ye, C.M. Wai, Synthesizing silver halide nanoparticles in supercritical carbon dioxide utilizing a water-in-CO2 microemulsion, Chemical Communications (2000) 2353–2354. https://doi.org/10.1039/b005924m.

[98] E. Reverchon, R. Adami, Nanomaterials and supercritical fluids, Journal of Supercritical Fluids 37 (2006) 1–22. https://doi.org/10.1016/j.supflu.2005.08.003.

[99] H. Ohde, F. Hunt, C.M. Wai, Synthesis of silver and copper nanoparticles in a water-in-supercritical-carbon dioxide microemulsion, Chemistry of Materials 13 (2001) 4130–4135. https://doi.org/10.1021/cm010030g.

[100] M. Ohde, H. Ohde, C.M. Wai, Catalytic hydrogenation of arenes with rhodium nanoparticles in a water-in-supercritical CO2 microemulsion, Chemical Communications 2 (2002) 2388–2389. https://doi.org/10.1039/b205993m.

[101] L. Du, J.Y. Kelly, G.W. Roberts, J.M. DeSimone, Fluoropolymer synthesis in supercritical carbon dioxide, Journal of Supercritical Fluids 47 (2009) 447–457. https://doi.org/10.1016/j.supflu.2008.11.011.

[102] L. Cao, L. Chen, X. Chen, L. Zuo, Z. Li, Synthesis of smart core-shell polymer in supercritical carbon dioxide, Polymer (Guildf) 47 (2006) 4588–4595. https://doi.org/10.1016/j.polymer.2006.04.039.

[103] S. Do Yeo, E. Kiran, Formation of polymer particles with supercritical fluids: A review, Journal of Supercritical Fluids 34 (2005) 287–308. https://doi.org/10.1016/j.supflu.2004.10.006.

[104] C.D. Wood, A.I. Cooper, J.M. Desimone, Green synthesis of polymers using supercritical carbon dioxide, Curr Opin Solid State Mater Sci 8 (2004) 325–331. https://doi.org/10.1016/j.cossms.2005.02.001.

[105] N. Budisa, D. Schulze-Makuch, Supercritical carbon dioxide and its potential as a life-sustaining solvent in a planetary environment, Life 4 (2014) 331–340. https://doi.org/10.3390/life4030331.

[106] K. Harrison, J. Goveas, K.P. Johnson, E.A. O'Rear, Water-in-Carbon Dioxide Microemulsions with a Fluorocarbon–Hydrocarbon Hybrid Surfactant, Langmuir 10 (1994) 3536–3541. https://doi.org/10.1021/la00022a028.

[107] T.A. Hoefling, R.M. Enick, E.J. Beckman, Microemuisions in near-critical and supercritical CO2, Journal of Physical Chemistry 95 (1991) 7127–7129. https://doi.org/10.1021/j100172a006.

[108] D. Ribar, T. Rijavec, I. Kralj Cigić, An exploration into the use of Hansen solubility parameters for modelling reversed-phase chromatographic separations, J Anal Sci Technol 13 (2022). https://doi.org/10.1186/s40543-022-00322-9.

[109] E. Yilmaz, M. Soylak, Type of green solvents used in separation and preconcentration methods, INC, 2020. https://doi.org/10.1016/B978-0-12-818569-8.00005-X.

[110] M. Tobiszewski, J. Namieśnik, F. Pena-Pereira, Environmental risk-based ranking of solvents using the combination of a multimedia model and multi-criteria decision analysis, Green Chemistry 19 (2017) 1034–1042. https://doi.org/10.1039/c6gc03424a.

[111] P. Raveendran, Y. Ikushima, S.L. Wallen, Polar attributes of supercritical carbon dioxide, Acc Chem Res 38 (2005) 478–485. https://doi.org/10.1021/ar040082m.

[112] N. Zachmann, M. Petranikova, B. Ebin, Electrolyte recovery from spent Lithium-Ion batteries using a low temperature thermal treatment process, Journal of Industrial and Engineering Chemistry 118 (2023) 351–361. https://doi.org/10.1016/j.jiec.2022.11.020.

[113] N. Katayama, T. Kawamura, Y. Baba, J.I. Yamaki, Thermal stability of propylene carbonate and ethylene carbonate-propylene carbonate-based electrolytes for use in Li

cells, J Power Sources 109 (2002) 321–326. https://doi.org/10.1016/S0378-7753(02)00075-7.

[114] P. Jakóbczyk, M. Bartmański, E. Rudnicka, Locust bean gum as green and water-soluble binder for LiFePO4 and Li4Ti5O12 electrodes, J Appl Electrochem 51 (2021) 359–371. https://doi.org/10.1007/s10800-020-01496-z.

[115] B. Kumar, R. Priyadarshi, Sauraj, F. Deeba, A. Kulshreshtha, K.K. Gaikwad, J. Kim, A. Kumar, Y.S. Negi, Nanoporous sodium carboxymethyl cellulose-g-poly (Sodium acrylate)/fecl3 hydrogel beads: Synthesis and characterization, Gels 6 (2020) 1–11. https://doi.org/10.3390/gels6040049.

[116] A. Pettignano, A. Charlot, E. Fleury, Solvent-free synthesis of amidated carboxymethyl cellulose derivatives: Effect on the thermal properties, Polymers (Basel) 11 (2019). https://doi.org/10.3390/polym11071227.

[117] A.J. de Jesus Silva, M.M. Contreras, C.R. Nascimento, M.F. da Costa, Kinetics of thermal degradation and lifetime study of poly(vinylidene fluoride) (PVDF) subjected to bioethanol fuel accelerated aging, Heliyon 6 (2020). https://doi.org/10.1016/j.heliyon.2020.e04573.

[118] Z.X. Xu, C.X. Zhang, Z.X. He, Q. Wang, Pyrolysis Characteristic and kinetics of Polyvinylidene fluoride with and without Pine Sawdust, J Anal Appl Pyrolysis 123 (2017) 402–408. https://doi.org/10.1016/j.jaap.2016.10.027.

[119] A.E. Andreatta, L.J. Florusse, S.B. Bottini, C.J. Peters, Phase equilibria of dimethyl sulfoxide (DMSO) + carbon dioxide, and DMSO + carbon dioxide + water mixtures, Journal of Supercritical Fluids 42 (2007) 60–68. https://doi.org/10.1016/j.supflu.2006.12.015.

[120] F. Zahran, J. Morère, A. Cabañas, J.A.R. Renuncio, C. Pando, Role of excess molar enthalpies in supercritical antisolvent micronizations using dimethylsulfoxide as the polar solvent, Journal of Supercritical Fluids 60 (2011) 45–50. https://doi.org/10.1016/j.supflu.2011.02.015.

[121] H. Saba, X. Zhu, Y. Chen, Y. Zhang, Determination of physical properties for the mixtures of [BMIM]Cl with different organic solvents, Chin J Chem Eng 23 (2015) 804–811. https://doi.org/10.1016/j.cjche.2014.06.039.

[122] A.D. André, A.M. Teixeira, P. Martins, Influence of DMSO Non-Toxic Solvent on the Mechanical and Chemical Properties of a PVDF Thin Film, Applied Sciences (Switzerland) 14 (2024). https://doi.org/10.3390/app14083356.

[123] Y. Zhao, W. Yang, Y. Zhou, Y. Chen, X. Cao, Y. Yang, J. Xu, Y. Jiang, Effect of crystalline phase on the dielectric and energy storage properties of poly(vinylidene fluoride), Journal of Materials Science: Materials in Electronics 27 (2016) 7280–7286. https://doi.org/10.1007/s10854-016-4695-y.

[124] X. Cai, T. Lei, D. Sun, L. Lin, A critical analysis of the α, β and γ phases in poly(vinylidene fluoride) using FTIR, RSC Adv 7 (2017) 15382–15389. https://doi.org/10.1039/c7ra01267e.

[125] Y. Bormashenko, R. Pogreb, O. Stanevsky, E. Bormashenko, Vibrational spectrum of PVDF and its interpretation, Polym Test 23 (2004) 791–796. https://doi.org/10.1016/j.polymertesting.2004.04.001.

[126] T. Nishiyama, T. Sumihara, E. Sato, H. Horibe, Effect of solvents on the crystal formation of poly (vinylidene fluoride) film prepared by a spin-coating process, Polym J 49 (2017) 319–325. https://doi.org/10.1038/pj.2016.116.

[127] Z. Huang, J. Jiang, G. Xue, D. Zhou, β-Phase Crystallization of Poly (vinylidene fluoride) in Poly (vinylidene fluoride)/ Poly (ethyl methacrylate) Blends, (2019).

[128] J.-Y.L. Kuan-Ying Chan, Chia-Ling Li, Da-Ming Wang, Formation of Porous Structures and Crystalline Phases in Poly (vinylidene fluoride) Membranes Prepared with Solvent Polarity, Polymers (Basel) 15 (2023) 1314.

[129] N.D. Govinna, I. Sadeghi, C. Schick, A. Asatekin, P. Cebe, Crystallization kinetics, polymorphism fine tuning, and rigid amorphous fraction of poly(vinylidene fluoride) blends, Polymer Crystallization 4 (2021). https://doi.org/10.1002/pcr2.10205.

[130] R. Morales-Cerrada, V. Ladmiral, F. Gayet, C. Fliedel, R. Poli, B. Améduri, Fluoroalkyl pentacarbonylmanganese(I) complexes as initiators for the radical (co)polymerization of fluoromonomers, Polymers (Basel) 12 (2020). https://doi.org/10.3390/polym12020384.

[131] S.G. Lee, J.W. Ha, I.J. Park, S.B. Lee, J.D. Lee, Synthesis of poly(vinylidene fluoride-co-hexafluoropropylene), Polymer (Korea) 37 (2013) 74–79. https://doi.org/10.7317/pk.2013.37.1.74.

[132] V.S.D. Voet, M. Tichelaar, S. Tanase, M.C. Mittelmeijer-Hazeleger, G. Ten Brinke, K. Loos, Poly(vinylidene fluoride)/nickel nanocomposites from semicrystalline block copolymer precursors, Nanoscale 5 (2013) 184–192. https://doi.org/10.1039/c2nr32990e.

[133] J.H. Kim, H. Umeda, M. Ohe, S. Yonezawa, M. Takashima, Preparation of Pure LiPF6 using fluorine gas at room temperature, Chem Lett 40 (2011) 360–361. https://doi.org/10.1246/cl.2011.360.

[134] L. Williams, Determination of Hansen Solubility Parameter Values for Carbon Dioxide, Hansen Solubility Parameters (2007) 177–201. https://doi.org/10.1201/9781420006834.ch10.

[135] V.O.C. Concha, L. Timóteo, L.A.N. Duarte, J.O. Bahú, F.L. Munoz, A.P. Silva, L. Lodi, P. Severino, J. León-Pulido, E.B. Souto, Properties, characterization and biomedical applications of polyvinylidene fluoride (PVDF): a review, J Mater Sci 59 (2024) 14185–14204. https://doi.org/10.1007/s10853-024-10046-3.

[136] K. V. Pochivalov, A. V. Basko, A.N. Ilyasova, T.N. Lebedeva, M.Y. Yurov, S. V. Bronnikov, Experimental phase diagram for the PVDF – DMAc– water ternary system with new topology: Method of construction, thermodynamics, and structure formation of membranes, Polymer (Guildf) 282 (2023). https://doi.org/10.1016/j.polymer.2023.126152.

Appendix

Given that the reactor possesses a total internal volume of 11.5 ml, the residual volume available for CO_2 was calculated after subtracting the volumes occupied by the solvent and washed BM. The CO_2 density values were obtained from the NIST database, corresponding to 116.81, 173.62, 247.77, and 345.85 kg/m^3 at 70 ℃ under 60, 80, 100, and 120 bar, respectively. Similarly, at 120 bar, CO_2 densities were 808.93, 584.71, 345.85, and 264.95 kg/m3 for 30, 50, 70, and 90 ℃, respectively. The molecular weights used in the calculations were 44.04 g/mol for CO_2, 78.13 g/mol for DMSO, and 68.11 g/mol for the 1:1 DMSO:acetone mixture.

Acetone (≥ 99 %, EMPLURA®, Merck) possesses a density of 0.791 g/ml and a molecular weight of 58.08 g/mol, while dimethyl sulfoxide (≥ 99.9 %, ACS reagent, Sigma-Aldrich) exhibits a density of 1.10 g/ml and a molecular weight of 78.13 g/mol. A 50:50 vol% mixture of these solvents yields an estimated density of 0.9455 g/ml, as calculated using Eq. 1.

$$\rho_{mix} = \frac{V1.\rho1+V2.\rho2}{V1+V2} \quad (1)$$